Resistance and Seakeeping Optimization of a Naval Destroyer by Multi-Fidelity Methods

Andrea Serani, Simone Ficini, Riccardo Broglia, Matteo Diez
National Research Council
Institute of Marine Engineering
ITALY

Gregory Grigoropoulos, Chris Bakirtzogou George Papadakis
National Technical University of Athens
GREECE

Omer Goren, Devrim B. Danisman, Hayriye Pehlivan Solak, Şıhmehmet Yıldız, Melike Nikbay
Istanbul Technical University
TURKEY

Thomas Scholcz, Joy Klinkenberg
Maritime Research Institute Netherlands (MARIN)
THE NETHERLANDS

Keywords: Workshop, Multi-fidelity methods, Global optimization, Computational fluid dynamics, Ship hydrodynamics

ABSTRACT

The paper presents and discusses the so-called L3 sea benchmark problems used to develop and assess multi-fidelity optimization methods for military vehicle design within the AVT-331 Research Task Group on "Goal-driven, multi-fidelity approaches for military vehicle system-level design." The hull-form design (bare hull) of the DTMB 5415 model (an open-to-public concept used in the development of the DDG-51, the lead vessel of the Arleigh Burke-class guided missile destroyers) is addressed for optimal resistance and seakeeping performance in calm water, regular/irregular waves, and formulated as a global optimization problem. The design performance is assessed using a variety of physical models and solvers (from Reynolds-Averaged Navier Stokes equations to potential flow models), and spatial discretizations, which are combined together in dedicated multi-fidelity frameworks developed by the AVT-331 Sea Team. Benchmark problems description, design parameterization methods, physical models and solvers are presented and discussed, as well as multi-fidelity approaches and example results. The present effort highlights how the dimensionality of the optimization problem may be a critical issue for the surrogate model training. Nevertheless, it is shown how the proposed multi-fidelity approaches are able to achieve significant design performance improvements, even if only a few high-fidelity computations are used, with a ratio between the number of high- and low-fidelity evaluations required to solve the global optimization problem as low as nearly 1/50. Finally, the challenges arisen during the process are discussed and future research directions outlined.

1 INTRODUCTION

The design process of novel vessel is experiencing a methodological revolution, due to development of ever fast and powerful high performance computing (HPC) systems and efficient simulation-driven design

Table 5-1: DTMB 5415 main particulars.

Description	Symbol	Unit	Full scale	Model scale
Displacement	∇	tonnes	8,437	0.549
Length between perpendiculars	L_{pp}	m	142.0	5.720
Beam	B	m	18.90	0.760
Draft	T	m	6.160	0.248
Longitudinal center of gravity	LCG	m	71.60	2.884
Vertical center of gravity	VCG	m	1.390*	0.056*
Bridge longitudinal location	B_x	m	44.00†	1.772†
Bridge vertical location	B_z	m	24.75‡	0.997‡
Flight deck longitudinal location	D_x	m	132.0†	5.317†
Flight deck vertical location	D_z	m	13.00‡	0.524‡
Roll radius of gyration	K_{xx}	–	$0.40B$	
Pitch radius of gyration	K_{yy}	–	$0.25L_{\mathrm{pp}}$	
Yaw radius of gyration	K_{zz}	–	$0.25L_{\mathrm{pp}}$	

* Above the water line; † From bow; ‡ Above the keel

optimization (SDDO) frameworks. Generally, the accuracy of SDDO solutions requires high-fidelity and therefore computationally expensive computer simulations, such as high-fidelity computational fluid dynamics (CFD). As an example, a CFD-based statistically significant evaluation of ship performance in irregular seaways may require up to 1M CPU hours on HPC systems [1]. The computational cost required to evaluate design objectives and constraints further increases if multi-disciplinary/multi-physics, multi-point, and multi-objective problems need to be addressed, such as in the hydro-structural optimization of vessels at multiple speeds and conditions. Consequently and despite the availability of powerful HPC systems, the extensive use of high-fidelity simulation tools can be impractical in ship design optimization, especially when high-dimensional design spaces are explored for global optima.

Multi-fidelity (MF) approaches have shown their potential in alleviating the computational cost associated to the solution of high-fidelity SDDO problems, by combining multiple information sources, such as multiple physical models and solvers, space/time discretizations, levels of physical coupling. Nevertheless, the full potential and application domain of MF methods are still subject of discussion in the SDDO community, as MF methods feature a great number of different approaches, settings, and applications. For these reasons, one of the main goals of the AVT-331 on "Goal-driven, multi-fidelity approaches for military vehicle system-level design" is to rigorously address the capability of MF methods to solve efficiently and effectively design optimization problems for military vehicles. To this aim, the Task Group proposed the use of three types of benchmark problems for the assessment of MF methods, characterized by different levels of complexity, namely L1 (analytic problems), L2 (simple problems of engineering/vehicle relevance), and L3 [2]. L3 problems use partial differential equations solutions, exhibit physical coupling of two or more disciplines/systems, are affected by moderate to large numerical errors/uncertainties, have a large computational cost, and address vehicle-level engineering models. Their solution in a timely and affordable way is the final goal of MF approaches in AVT-331.

The objective of the present work is to present and discuss the AVT-331 Sea Team effort in solving the most complex type of problems, namely the L3 sea benchmark problems. These pertain to the hull-form optimization of a destroyer-type vessel for reduced resistance and increased seakeeping performance. Three global optimization problems are defined and addressed, covering calm-water and wave conditions, single- and

multi-point optimization. The DTMB 5415 model is used as a parent design, which is an open-to-public concept used in the development of the DDG-51, the lead vessel of the Arleigh Burke-class guided missile destroyers. The DTMB 5415 has been widely used in the community for computational and experimental studies, as well as in earlier AVT efforts. Different combinations of problem formulations, design space parameterizations, physical models and numerical solvers, and finally MF approaches are investigated here. Specifically four MF optimization frameworks are developed and tested by the AVT-331 Sea Team members and are here presented and discussed.

The focus of the paper is on discussing the ability of MF approaches to achieve high-fidelity globally optimal design decisions with only a few high-fidelity evaluations, therefore saving computational time and cost. It is worth noting that, although a direct comparison of MF framework capabilities and results is of certain interest to the community, when dealing with L3 type of problems (at least for the sea case) this encounters a number of barriers, spanning from CAD (computer aided design) and CFD tools availability and licences associated to proprietary software, to heterogeneous availability of CPU hours and men power across Team Members. For these reasons, L1 and L2 benchmark problems are devoted to closer comparisons of MF approaches and results, whereas L3 benchmark problems (at least for the sea case) are dedicated to demonstrating MF methods capabilities for more complex industrial problems, albeit with limited comparison.

2 PROBLEM STATEMENT

The L3 sea benchmark problem consists in the hull-form optimization of the DTMB 5415 model geometry with no appendages (bare hull).This has been widely used for towing tank experiments [3], CFD studies [4], and hull-form optimization [5]. The DTMB 5415 model (both bare hull and its appended variants) have been used also as a test case for, among others, AVT-204 [6] and AVT-252 [7] respectively on deterministic and stochastic design optimization methods for military vehicles and AVT-280 [1] on prediction capabilities of ships' large amplitude motions in heavy weather. The model main particulars (bare hull) are summarized in Table 5-1, where the length parameter L_{pp} is calculated from the fore perpendicular to the transom bottom edge.

The general design optimization reads

$$\begin{array}{rlll} \text{minimize} & f_k(\mathbf{x}) & \text{with} & k = 1, \ldots, K \\ \text{subject to} & h_i(\mathbf{x}) = 0 & \text{with} & i = 1, \ldots, I \\ \text{and to} & g_j(\mathbf{x}) \leq 0 & \text{with} & j = 1, \ldots, J \\ & \mathbf{x}_l \leq \mathbf{x} \leq \mathbf{x}_u & & \end{array} \tag{5-1}$$

where $\mathbf{x}$ is the design variable vector (related to shape parameterization), with $\mathbf{x}_l$ and $\mathbf{x}_u$ its lower and upper bounds, f_k are the objective functions ($k = 1$ means single-objective problem, whereas $k > 1$ means multi-objective), h_i are the equality constraints, and finally g_j are the inequality constraints.

Three optimization problems are defined, considering two main sets of conditions, namely calm water and regular/irregular waves. Design objectives include merit factors associated to both resistance (in calm water and waves) and seakeeping (motions in waves). Physical coupling is considered of hydrodynamics with rigid body equations of motion. All the three problems use an equality constraint for the L_{pp}, whereas inequality constraints are given for displacement, beam, draft, and the volume reserved for the sonar in the bow dome. Specifically, the displacement have to be greater or equal to the parent hull, whereas $\pm 5\%$ variation of beam and draft is allowed.

Problem 1 pertains to the single-objective ($k = 1$) minimization of the total resistance R_T in calm water at $\mathrm{Fr} = 0.28$ (corresponding to 20kn at full scale),

$$\text{minimize} \quad f_1(\mathbf{x}) = R_\mathrm{T}(\mathbf{x}) \tag{5-2}$$

Problem 2 is a multi-objective problem ($k = 2$) and pertains to the resistance reduction and seakeeping performance improvement in regular head waves at $\mathrm{Fr} = 0.28$ (20kn at full scale):

$$\begin{aligned} &\text{minimize} \quad f_1(\mathbf{x}) = \bar{R}_\mathrm{T}(\mathbf{x}) = \tfrac{1}{T_e}\int_0^{T_e} R_\mathrm{T}(\mathbf{x},t)\mathrm{d}t \\ &\text{minimize} \quad f_2(\mathbf{x}) = \mathrm{SMF}(\mathbf{x}) = \tfrac{1}{3}\tfrac{\mathrm{RMS}(v_d)}{\mathrm{RMS}(v_{d,0})} + \tfrac{1}{3}\tfrac{\mathrm{RMS}(a_b)}{\mathrm{RMS}(a_{b,0})} + \tfrac{1}{3}\tfrac{\mathrm{RMS}(\theta)}{\mathrm{RMS}(\theta_0)} \end{aligned} \tag{5-3}$$

where T_e is the encounter wave period. Regular waves are characterized by the wavelength $\lambda/L_\mathrm{pp} = 1.2$ and a steepness $H/\lambda = 1/30$. The seakeeping performance is assessed by a seakeeping merit factor (SMF) that uses the root mean square (RMS) of the vertical velocity at the flight deck v_d, the vertical acceleration at the bridge a_b, and the pitch angle θ. Subscript '0' refers to parent-hull values.

Problem 3 is taken from AVT-204 [6] and is a multi-point (18kn and 30kn, corresponding to $\mathrm{Fr} = 0.25$ and 0.41, respectively) multi-objective optimization ($k = 2$) considering calm-water resistance minimization and seakeeping performance improvement in irregular waves:

$$\begin{aligned} &\text{minimize} \quad f_1(\mathbf{x}) = 0.85\ \tfrac{R_T}{R_{T_0}}\Big|^{18\mathrm{kn}} + 0.15\ \tfrac{R_T}{R_{T_0}}\Big|^{30\mathrm{kn}} \\ &\text{minimize} \quad f_2(\mathbf{x}) = 0.5\ \tfrac{\mathrm{RMS}(a_b)}{\mathrm{RMS}(a_{b,0})}\Big|_{180\mathrm{deg}}^{30\mathrm{kn}} + 0.5\ \tfrac{\mathrm{RMS}(\varphi)}{\mathrm{RMS}(\varphi_0)}\Big|_{30\mathrm{deg}}^{18\mathrm{kn}} \end{aligned} \tag{5-4}$$

where φ is the roll angle at 18 kn in stern long-crested waves with 30 deg heading. The wave conditions corresponds to sea state 5, using the Bretschneider spectrum with a significant wave height of 3.25 m and modal period of 9.7 s. Subscript '0' refers to parent-hull values.

3 HULL-FORM PARAMETERIZATION

Four hull-form parameterization approaches are used, including free-form deformation, Akima's surface generation, hull blending, and a computer-aided design (CAD) parametric modeling approach. Details are provided in the following subsections. Finally, a brief description of design-space dimensionality reduction via parametric model embedding (PME) [8] is also provided.

3.1 Free-Form Deformation

FFD [9] is used to generate design variants and modify the associated computational grid. The number and coordinates of CPs $\mathbf{c}_{ijk}$, defined as lattice nodes, are chosen to generate both local and global modifications of the hull, based on earlier experience within AVT-204 [6]. Specifically, the design space is formed by $M = 22$ design variables; the demi-hull is put in a lattice of $9 \times 3 \times 3$ nodes in the $\xi_1\xi_2\xi_3$ reference system (note that the FFD lattice perfectly fit the demi-hull maximum dimension); only 21 nodes are active (see blue sphere in

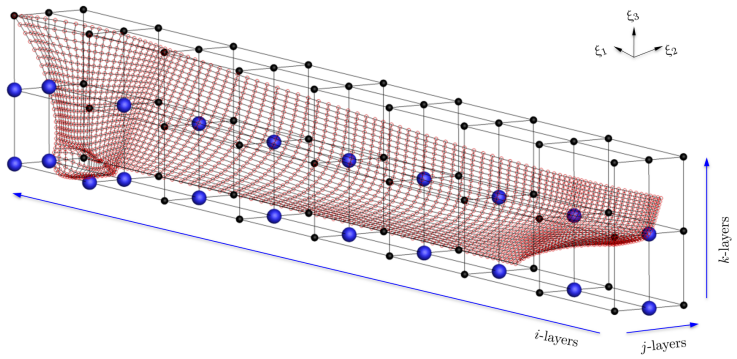

Figure 5-1: FFD parameterization.

Fig. 5-1), all with only one degrees of freedom (DoF), expect for one that has 2 DoF; the number of CPs used in $\hat{\mathbf{T}}_1$, $\hat{\mathbf{T}}_2$, and $\hat{\mathbf{T}}_3$ directions are t_1, t_2, and t_3, respectively; the shape modification is achieved by interpolating the CPs' modification over the embedding space. The interpolation can be performed using different polynomial bases. Herein, a tensor product of trivariate Bernstein polynomial is used

$$\boldsymbol{\delta}(\boldsymbol{\xi}, \mathbf{u}) = \sum_{i=0}^{t_1} \sum_{j=0}^{t_2} \sum_{k=0}^{t_3} b_{i,t_1}(\alpha) b_{j,t_2}(\beta) b_{k,t_3}(\gamma) \mathbf{c}_{ijk}(\mathbf{u}) - \boldsymbol{\xi} \tag{5-5}$$

where $\delta(\boldsymbol{\xi})$ is the shape modification vector, with $\boldsymbol{\xi}$ the coordinates of the discretized shape and $b_{v,r}(\chi)$ a generic Bernstein basis polynomials. Detailed description of DoF and associated design variables can be found in [8].

3.2 Akima's Surface Generation

Akima's [10] surface generation method, from a set of scattered points (See Fig. 5-2), is used to define the hull surface related to these coefficients; that is, by using x and z coordinates of a particular point, modified values ($\mathbf{y}^{(i)}$) of the control points are obtained as:

$$\mathbf{y}^{(i)} = \mathbf{y}^{(o)} \cdot \mathbf{C}_r^{(i)}(\mathbf{x}^{(o)}, \mathbf{z}^{(o)}) \tag{5-6}$$

where (o) and (i) denote the original form and the i^{th} modified form in the Design of Experiments, respectively. Further to have a finer mesh, the relaxation coefficients, $\mathbf{C}_r^{(i)}$ (randomly assigned value at the control points), for other intermediate (interpolation) points are obtained by interpolation using the relaxation coefficients defined at the control points. In this approach, fairing problem could be eliminated by imposing a set of fairness criteria. Since there is no precisely defined fairness criterion in the present work, no fairing on the wetted surface of the

Figure 5-2: Akima's surface parameterization.

hull is applied. Note that C_r value is kept between 0.9 and 1.1 which is also subjected to the beam allowance limited to $\pm 5\%$ change only. Ultimately, the hull generation code creates new sections by interpolating the modified waterlines to prepare input data for the wave resistance code explained in the following section.

3.3 Hull Blending

A hull-blending technique is used to parameterise the hull shape. A small number of basis hull designs are chosen which define the scope of the deformations. Let H_0 denote the "original" hull shape. The other basis shapes are then denoted by H_1, H_2,...,H_N, each characterising a type of deformation. Each basis shape H_n is defined by N_c control points $\mathbf{c}_{n,i}$ of a B-spline surface. The parameterised control points are then obtained by linear interpolation on the control points of the basis designs:

$$\mathbf{c}_i(\mathbf{x}) = \mathbf{c}_i([x_1, x_2, ..., x_N]) = \mathbf{c}_{0,i} + \sum_{n=1}^{N} x_n(\mathbf{c}_{n,i} - \mathbf{c}_{0,i}) \quad \text{for} \quad i = 1, 2, \ldots, N_c \tag{5-7}$$

Each linear interpolation coefficient represents a contribution of a certain shape deformation of the corresponding basis shape in the "hull-blend". Using this definition, the design space is a N-dimensional unit hypercube with the original hull design corresponding to $\mathbf{x} = \mathbf{0}$ and the other basis shapes corresponding to the corner points of this cube. The basis shapes used here are given in Figure 5-3.

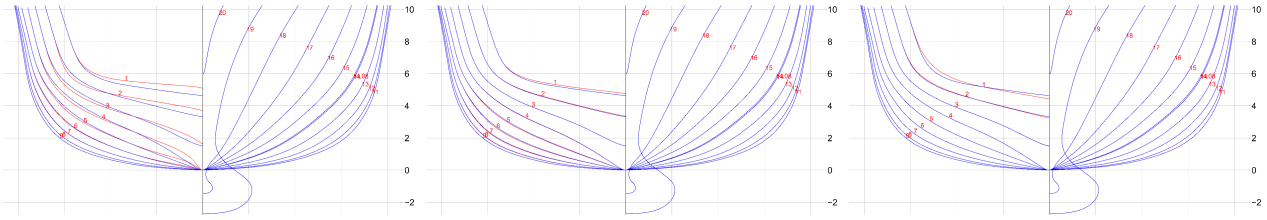

(a) H_1: Aft buttocks S-shape *(b) H_2: Transom immersion* *(c) H_3: V-shape*

Figure 5-3: Blending Parameterization Basis Hull Shapes.

3.4 CAD Parametric Modeling

The CAESES software is used for the parametric design and variation of the parent hull. The initial geometry is represented by a set of basic curves providing topological information in the longitudinal direction (design waterline, centerline, deck-line) and a set of 19 section curves. All of them are either F-splines, or B-splines. The geometry is split into three regions: the main hull, the sonar dome, and the skeg, assigning specific design variables for each of them. The main hull part was split into five lofted surfaces, involving skeg surface too. The separation of the hull to main and fore part is related to the selected way of approximating the initial surfaces and to the fact that the design variables for the main hull form concerned only its fore part. Thus, the fore part of the hull form was split into six parts, and five design variables of the lower dome's surface were employed.

A total number of ten design variables is employed, five of which are used to define the sonar dome. The range of variation has been selected to lead to realistic hull forms and smooth lines. In addition, upper and

Table 5-2: Parametric model design space definition (full scale size).

#	Description	Lower bound [m]	Upper bound [m]
1	Maximum Beam at Station 0	6.5	7.2
2	Maximum beam of sonar dome	2.9	3.6
3	Angle of Entrance	185.3	195.3
4	Wedge Depth	0.0	0.6
5	Maximum Beam at WL	9.0	9.8
6	Aft longitudinal position of sonar dome's lower profile	125.8	126.5
7	Forward longitudinal position of sonar dome's lower profile	140.8	142.5
8	Height of Skeg	1.5	2.5
9	Longitudinal position of sonar dome's maximum beam	135.8	138.0
10	Sonar dome's tip elevation (for the most forward point of sonar dome's length)	-1.7	-1.3

lower boundaries comply with the geometrical constraints as defined. Table 5-2 provides the range of the design variables and their values for the parent hull form.

3.5 Parametric Model Embedding

PME method extends the design-space dimensionality reduction formulation, based on the Karhunen-Loéve expansion (KLE) of the shape modification vector, presented in [11], using a generalized feature space that includes shape modification and design variables vectors together with a generalized inner product, aiming at resolving a prescribed design variability by properly selecting the latent dimensionality. The method provides a direct way to return to the original parameterization from the reduced dimensionality latent space, allowing therefore for the super-parametrization of the original parametric model. PME can be directly integrated in CAD software and SDDO toolchain, avoiding the necessity to implement a new shape modification method based on the geometric component of the KLE eigenvectors and also easily enabling a search for the optimum within the original design bounds. Details of PME formulation and implementation can be found in [8].

4 PHYSICAL MODELS AND NUMERICAL SOLVERS

Different governing equations and solvers, with different computational grid sizes, are considered for the MF solution of the design problems. A brief description of models and codes is included in the following.

4.1 CFDShip-Iowa

CFDShip-Iowa V4.5 code [12] has been developed at the University of Iowa over the past 30 years. CFDShip-Iowa V4.5 is an incompressible RANS/DES solver designed for ship hydrodynamics. The equations are solved in an inertial coordinate system, either fixed to a ship or other frame moving at constant speed or in the earth system. The free-surface is modelled with a single-phase capturing approach, meaning that only

the water flow is solved, enforcing kinematic and dynamic free-surface boundary conditions on the interfaces. Arbitrary free-surface topologies can be predicted, with the limitation that pressurized closed air/water packets (bubbles) cannot be simulated. It uses structured multiblock grids, and has overset capabilities. Capabilities include 6DoF motions, several turbulence models, moving control surfaces, multi-objects, advanced controllers, propulsion models, incoming waves and winds, bubbly flow, and fluid-structure interaction. In the present study the URANS equations are solved in the ship coordinate system. The turbulence is computed by the isotropic Menter's blended $k-\omega/k-\epsilon$ (BKW) model with shear stress transport (SST). A second order upwind scheme is used to discretize the convective terms of momentum equations. Pressure implicit with splitting of operators (PISO) loop for pressure/velocity coupling is used. For a high performance parallel computing, an MPI-based domain decomposition approach is used, where each decomposed block is mapped to one processor. The code SUGGAR runs as a separate process from the flow solver to compute interpolation coefficients for the overset grid, which enables CFDShip-Iowa to take care of 6DoF with a motion controller at every time step.

4.2 OpenFOAM

The open-source Navier-Stokes solver OpenFOAM is able to solve a wide range of problems in fluid dynamics and is utilized presently to calculate the total resistance of ship hulls in calm water. The solver employs earth and body fixed Cartesian coordinate system, with z-axis upward positive and the ship is free to sink and trim. The governing equations are continuity and Reynolds Averaged Navier-Stokes equations. The volume of fluid (VoF) approach is used to model the two flow phases of water and air above the still water level. The SST $k-\omega$ turbulence model is employed in order to solve the turbulence equations, where ω represents the specific dissipation rate. The first-order implicit (Euler) scheme is applied to discretize the unsteady term in Navier-Stokes equations. PIMPLE algorithm, a combination of PISO and SIMPLE (Semi Implicit Methods Pressure Linked Equations) algorithms, is used to solve the pressure-velocity coupling.

4.3 ReFRESCO

ReFRESCO is a viscous-flow CFD code that solves multiphase (unsteady) flows using the incompressible Navier-Stokes equations, complemented with turbulence and cavitation models [13]. The equations are discretised using a finite-volume approach and in strong-conservation form. A pressure-correction equation based on the SIMPLE algorithm is used to ensure mass conservation [14]. At each implicit time step, the non-linear system for velocity and pressure is linearised using Picard's method. A segregated or coupled approach may be used. The code is parallelised using MPI and runs on Linux workstations and HPC clusters. Due to specific numerical schemes, ReFRESCO can deal robustly with low up to high (full-scale) Reynolds numbers, permitting the accurate estimation of scale effects. The face-based implementation permits the handling of grids from several different grid-generation packages. State-of-the-art CFD features such as moving, sliding and deforming grids, as well automatic grid adaptation (refinement and/or coarsening) are also available. Both 6DOF rigid-body, and flexible-body (fluid-structure interaction) simulations, can be performed. For turbulence modelling, both traditional RANS and Scale-Resolving Simulations (SRS) models such as SAS/DDES/IDDES/XLES, PANS and LES can be used. Noise predictions can be made using an acoustic analogy module. Couplings with propeller models (RANS- BEM coupling), fast-time simulation tools (XMF) and wave generation potential flow codes (OceanWave3D, SWASH) are implemented.

4.4 MaPFlow

It is an NTUA in-house (U)RANS cell-centered solver, that can use both structured and unstructured grids, capable of solving compressible flows, as well as fully incompressible flows using the artificial compressibility method. For the reconstruction of the flow field, a 2nd order piecewise linear interpolation scheme is used. The limiter of Venkatakrishnan [15] is utilized when needed. The viscous fluxes are discretized using a central 2nd order scheme. Turbulence closures implemented on MaPFlow include the one-equation turbulence model of Spalart [16] as well as the two-equation turbulence model of Menter ($k-\omega$ SST) [17]. Regarding laminar to turbulent transition modeling, the correlation $\gamma - \mathrm{Re}\theta$ model of Langtry and Menter [18] has been implemented. MaPFlow can handle both steady and unsteady flows. Time integration is achieved in an implicit manner permitting large CFL numbers. The unsteady calculations use a 2nd order time accurate scheme combined with the dual time-stepping technique to facilitate convergence. MaPFlow can handle moving/deforming geometries through the arbitrary Eulerian Lagrangian formulation. Free surface is treated via the VoF method, where two phase flows are described by two immiscible fluids with their interface being defined implicitly as a discontinuity in the density field. The system of equations is solved in a non-segregated manner, utilizing the Kunz Preconditioner, as discussed by Yue and Wu [19], to remove density dependencies from the system's eigenvalues

4.5 WARP

The WAve Resitance Program (WARP) is a linear potential flow code developed at CNR-INM (formerly INSEAN). Wave resistance computations are based on the on Dawson (double-model) linearization [20], whereas the frictional resistance is estimated using a flat-plate approximation, based on the local Reynolds number [21]. The resistance is evaluated by integration of the pressure and friction over the body surface. The steady 2DoF (sinkage and trim) equilibrium is achieved by iteration of the flow solver and the body equation of motion. Details of equations, numerical implementations, and validation of the numerical solver are given in [22].

4.6 ITU-Dawson

ITU-Dawson is an ITU in-house code, which utilizes the usual assumptions for the non-lifting potential flow. Wave resistance analyses are carried out by ITU-Dawson and total resistance is determined by adding viscous resistance obtained from ITTC-1957 friction line accompanied with a computed form factor. Hull form definition is obtained from an IGS file, which is directly used in the discretization process, accomplished by a pre-processor of potential flow-solver. It calculates the unknown velocity potential by using a source/sink distribution over the panels — according to Hess and Smith's method — distributed on the wetted surface of the ship as well as on a portion of the free surface in the vicinity of the hull. The free surface condition is linearized according to low-Froude number theory and is satisfied by means of a numerical scheme introduced by Dawson [20]. In case of a transom stern, a wet transom boundary condition is imposed, discussed by Maisonneuve [23], and dry transom condition is imposed for Froude numbers greater than 0.35, studied by Cheng [24]. Actual (dynamic) sinkage and trim are applied to the hull by an iterative procedure.

4.7 SWAN2

The Ship Wave ANalysis software package for the hydrodynamics analyses was developed at MIT. It distributes quadrilateral panels over the ship hull and the free-surface to derive numerically the steady and unsteady free-surface potential flow around ships, using a three-dimensional Rankine Panel Method in the time domain. Only the calm water results are used in the present study. A batch file is used to integrate SWAN2 with the CAESES/FFW.

4.8 SMP

Finally, low fidelity seakeeping performance are evaluated by the Standard Ship Motion program (SMP), developed at the David Taylor Naval Ship Research and Development Center [25]. SMP provides a potential flow solution based on linearized strip theory. The 6DoF response of the ship is given, advancing at constant forward speed with arbitrary heading in both regular waves and irregular seas, as well as the longitudinal, lateral, and vertical responses at specified locations of the ship.

4.9 SPP-86

SPP-86 code has been developed in the Laboratory for Ship and Marine Hydrodynamics (LSMH) of NTUA to implement the Salvensen, Tuck and Faltinsen strip theory [26]. The code distributes Kelvin sources along the wetted part of each ship section following Frank method [27]. The estimated dynamic responses encompass vertical and lateral motions, velocities and accelerations at specific points for a variety of wave frequencies and heading angles.

5 MULTI-FIDELITY INTEGRATION METHODS

The MF integration methods proposed by the AVT-331 Sea Team are mainly based on surrogate models, such as multi-fidelity/source/level radial basis functions, Gaussian process/Kriging, as well as Artificial Neural Networks (ANN). The following subsection provides mathematical and methodological details of the proposed methods.

5.1 Stochastic Radial Basis Functions

Given a training set $\mathcal{T} = \{\mathbf{x'}_i, q(\mathbf{x'}_i)\}_{i=1}^{J}$ and normalizing the design-variables domain into a unit hypercube, the RBF prediction is here based on a power function kernel and reads [28]

$$h\left(\mathbf{x}, \tau\right) = \mathbb{E}[\mathbf{q}] + \sum_{j=1}^{\mathcal{K}} w_j \|\mathbf{x} - \mathbf{c}_j\|^{\tau}, \tag{5-8}$$

where w_j are unknown coefficients, $\mathbf{c}_j$ are $\mathcal{K}$ points in Γ called RBF centers, and $\tau \sim \text{unif}[\tau_{\min}, \tau_{\max}]$ is a stochastic tuning parameter that follows a uniform distribution. The range of τ is defined within $\tau_{\min} = 1$ and

$\tau_{\max} = 3$. The SRBF surrogate model $\widetilde{h}(\mathbf{x})$ is computed as the expected value (approximated by Monte Carlo) of h over τ [29]:

$$q(\mathbf{x}) \approx \widetilde{h}(\mathbf{x}) = \mathbb{E}_\tau [h(\mathbf{x}, \tau)] \approx \frac{1}{\Theta} \sum_{i=1}^{\Theta} h(\mathbf{x}, \tau_i), \tag{5-9}$$

where Θ is the number of samples for τ, here set equal to 100. In the present work, exact interpolation of the training set is imposed by setting $\mathcal{K} = J$ and the coefficients w_j are computed by solving

$$\mathbf{A}\mathbf{w} = (\mathbf{q} - \mathbb{E}[\mathbf{q}]) \tag{5-10}$$

with $\mathbf{w} = [w_1, \ldots, w_J]^\mathsf{T}$, $\mathbf{A}_{ij} = ||\mathbf{x}_i - \mathbf{c}_j||^\tau$ with $\mathbf{c}_j = \mathbf{x}'_j$, and $\mathbf{q} = [q(\mathbf{x}'_1), \ldots, q(\mathbf{x}'_\mathcal{J})]^\mathsf{T}$.

The uncertainty $U_{\widetilde{h}}(\mathbf{x})$ associated with the SRBF surrogate model prediction is quantified by the 95%-confidence band of the cumulative density function (CDF) of $h(\mathbf{x}, \tau)$ with respect to τ for fixed $\mathbf{x}$ as follows

$$U_{\widetilde{h}}(\mathbf{x}) = \mathrm{CDF}^{-1}(0.975; \mathbf{x}) - \mathrm{CDF}^{-1}(0.025; \mathbf{x}), \tag{5-11}$$

with

$$\mathrm{CDF}(\lambda; \mathbf{x}) \approx \frac{1}{\Theta} \sum_{i=1}^{\Theta} \mathcal{H}[\lambda - h(\mathbf{x}, \tau_i)], \tag{5-12}$$

where $\mathcal{H}(\cdot)$ is the Heaviside step function [30].

Finally, since the SRBF with power kernel has a low accuracy when extrapolating, both surrogate model prediction and the associated uncertainty are bounded (in the following denoted with the subscript 'b'). Specifically, when only one training point is available ($J = 1$), the surrogate model prediction and the associated uncertainty are set equal to the function value in the training point $q(\mathbf{x}')$ as follows

$$\widetilde{h}_b(\mathbf{x}) = q(\mathbf{x}'_i) \qquad \text{and} \qquad U_{\widetilde{h}_b}(\mathbf{x}) = q(\mathbf{x}'_i) \tag{5-13}$$

This approach is consistent with Eq. 5-9, where the expected value of the training set is added to the RBFs thus providing non-zero prediction when only one training point is available wackers2022improving. On the contrary, when $J > 1$ training points are available, the surrogate model prediction and the associated uncertainty are bounded only in regions of the domain far from these training points as follows

$$\widetilde{h}_b(\mathbf{x}) = \widetilde{h}(\mathbf{x})\,[1 - \sigma(r)] + \mathbb{E}[\mathbf{q}]\,\sigma(r) \qquad \text{and} \qquad U_{\widetilde{h}_b}(\mathbf{x}) = \min\left(U_{\widetilde{h}}, \mathbb{E}[\mathbf{q}]\right) \tag{5-14}$$

with σ a sigmoid-like function, used to provide a smooth transition between the SRBF prediction and the bounded prediction. Specifically, defining $\mathcal{R}$ as the smallest hyper-rectangle containing the training point coordinates $\{\mathbf{x}'\}_{i=1}^{J}$, whose edges are parallel to the Cartesian axis, the sigmoid-like function is defined as follows

$$\sigma(r) = \frac{1}{1 + \exp[\upsilon(r - \gamma)]}, \qquad \text{with} \qquad \upsilon = \frac{\alpha}{d_b + \epsilon} \qquad \text{and} \qquad \gamma = \beta(d_b + \epsilon) \tag{5-15}$$

where r is the Euclidean distance of $\mathbf{x}$ from the $\mathcal{R}$ boundaries and d_b is the Euclidean distance between the design variable boundaries and the boundary of $\mathcal{R}$.

Extending the definition of the training set to an arbitrary number L of fidelity levels as $\{\mathcal{T}_k\}_{k=1}^{L}$, with each $\mathcal{T}_k = \{(\mathbf{x}'_j, q_k(\mathbf{x}'_j))\}_{j=1}^{\mathcal{J}_k}$, the multi-fidelity approximation $\widehat{h}_k(\mathbf{x})$ of $q(\mathbf{x})$ reads [31], [32]

$$\widehat{h}_k(\mathbf{x}) := \widetilde{h}_L(\mathbf{x}) + \sum_{i=k}^{L-1} \widetilde{\varepsilon}_i(\mathbf{x}), \tag{5-16}$$

where $\widetilde{h}_L$ is the single-fidelity surrogate model associated to the lowest-fidelity training set (constructed as in Eq. (5-9)), and $\varepsilon_i(\mathbf{x})$ is the inter-level error surrogate with associated training set $\mathcal{E}_i = \{(\mathbf{y}, \phi - \widehat{h}_i(\mathbf{y})) \,|\, (\mathbf{y}, \phi) \in \mathcal{T}_{i-1}\}$.

Assuming that the uncertainty associated to the prediction of the lowest-fidelity $U_{\widetilde{h}_L}$ and inter-level errors $U_{\widetilde{\varepsilon}_i}$ as uncorrelated, the multi-fidelity approximation $\widehat{h}(\mathbf{x})$ of $q(\mathbf{x})$ and its uncertainty $U_{\widehat{h}}$ read

$$q(\mathbf{x}) \approx \widehat{h}(\mathbf{x}) = \widetilde{h}_L(\mathbf{x}) + \sum_{i=1}^{L-1} \widetilde{\varepsilon}_i(\mathbf{x}) \qquad U_{\widehat{h}}(\mathbf{x}) = \sqrt{U^2_{\widetilde{h}_L}(\mathbf{x}) + \sum_{i=1}^{L-1} U^2_{\widetilde{\varepsilon}_i}(\mathbf{x})}. \tag{5-17}$$

The multi-fidelity SRBF is dynamically updated by adding new training points. A new training point $\mathbf{x}^\star$ is identified based on acquisition function $\psi(\mathbf{x})$, here defined by the lower confidence bounding (LCB) criterion [33]. It aims to find points with large prediction uncertainty and small objective function value. Once $\mathbf{x}^\star$ is identified, to automatically select the fidelity level to sample, a fidelity selection vector $\boldsymbol{\varphi}$ is defined as follows

$$\boldsymbol{\varphi} \equiv \{U_{\widetilde{\varepsilon}_1}/\beta_1, ..., U_{\widetilde{\varepsilon}_{L-1}}/\beta_{L-1}, U_{\widetilde{f}_L}/\beta_L\}, \tag{5-18}$$

where $\beta_i = c_i/c_1$, $i = 1, ..., L$, with c_i the computational cost associated to the i-th level. Using non-nested training set, the i-fidelity level to sample is defined by identify the maximum value in $\boldsymbol{\phi}$ as follows

$$k = \text{maxloc}(\boldsymbol{\varphi}) \quad \text{with} \quad i = k \tag{5-19}$$

5.2 Kriging Partial Least Squares

Kriging Partial Least Squares (KPLS) is a modified version of Kriging derived by Bouhlel et al. [34] that uses partial least squares (PLS) approach and reduces the number of hyper parameters to be optimized while maintaining a successful estimation accuracy. Especially for high-dimensional problems KPLS becomes prominent method due to using the advantage of kernel constructed structure of PLS. The PLS coefficients are calculated using linear dependence between input and outputs and this relation is used in modified correlation function of inputs for deriving the KPLS method. A standard Gaussian correlation function and modified PLS-Gaussian correlation function are given in Eq. 5-20, respectively,

$$\prod_{l=1}^{nx} \exp\left(-\theta (x_l^{(i)} - x_l^{(j)})^2\right), \quad \prod_{k=1}^{h} \prod_{l=1}^{nx} \exp\left(-\theta_k (w_{*l}^{(k)} x_l^{(i)} - w_{*l}^{(k)} x_l^{(j)})^2\right) \qquad \forall \theta_l,\ \theta_k \in \mathbb{R}^+ \tag{5-20}$$

where w_* values represents PLS coefficients and the number of principal components h, usually does not exceeded 4 which is much lower than the dimension of the problem. By this way, the number of hyper parameters are reduced drastically when it is compared to Kriging surrogate model.

The rest of the implementation is the same as that of Kriging which is widely used as a stochastic surrogate modeling approach. Kriging, known as Gaussian Process (GP) regression, uses the interpolation of the input variables based on GP with zero mean driven by prior covariances. The covariance function r, used as squared exponential kernel function within the scope of this study, is given in Eq. 5-21

$$r(x, x'; \theta(\alpha, \beta)) = \alpha^2 \exp\left(-\frac{1}{2}\sum_{i=1}^{D}\frac{(x - x_i')^2}{\beta_i^2}\right) \tag{5-21}$$

Hyper-parameters $\theta(\alpha, \beta)$ and the noise variance σ are determined by maximizing the negative log-marginal-likelihood (NLML) equation given in Eq. 5-22

$$\mathcal{NLML}(\theta) = \frac{1}{2}y^T\mathbf{R}{-}1\mathbf{y} + \frac{1}{2}\log|\mathbf{R}| + \frac{N}{2}\log(2\pi) \qquad \text{with} \qquad \mathbf{R} = r(\mathbf{x}, \mathbf{x}; \theta) + \sigma^2\mathbf{I}. \tag{5-22}$$

where $\mathbf{R}$ is the covariance vector. The predicted value of the surrogate model is calculated as;

$$f(x^*) = r(x^*, x)\mathbf{R}^{-1}y \tag{5-23}$$

In order to use MF information in the prediction of the surrogate model, lineer auto-regressive approximation, derived by Kennedy O'Hagan [35], is used within the scope of this study. According to this model different fidelity levels are used in data fusion scheme which are assumed as linearly independent. By calculating the difference between the fidelities from corresponding data points, the MF prediction is calculated as

$$f_{MF}(x) = \rho f_F(x) + f_d(x) \tag{5-24}$$

with ρ a scaling factor, which is calculated based on the difference between fidelities, and $f_d(x)$ is the discrepancy function.

5.3 Augmented Expected Improvement-Based Kriging

The adaptive multi-fidelity Kriging method from [36] is implemented and tested, see [37]. The method is based on an augmented Expected Improvement (EI_α) function, which modifies the single-fidelity Expected Improvement (EI) function according to

$$\text{EI}_{\boldsymbol{\alpha}}(\mathbf{x}, l) = \text{EI}(\mathbf{x})\alpha_1(\mathbf{x}, l)\alpha_2(\mathbf{x}, l)\alpha_3(\mathbf{x}, l). \tag{5-25}$$

During the adaptive training method, the next point $\mathbf{x}_{n+1}$ at fidelity level l_{n+1} is computed from

$$(\mathbf{x}_{n+1}, l_{n+1}) = \underset{\mathbf{x}, l}{\text{argmax}}\,\text{EI}_{\boldsymbol{\alpha}}(\mathbf{x}, l), \tag{5-26}$$

with the factors α_1, α_2 and α_3 given by

$$\alpha_1(\mathbf{x}, l) = \text{cov}\left(f_1^p(\mathbf{x}), f_l^p(\mathbf{x})\right) \Big/ \left(\sqrt{\text{Var}(f_1^p(\mathbf{x}))}\sqrt{\text{Var}(f_l^p(\mathbf{x}))}\right) \tag{5-27}$$

$$\alpha_2(\mathbf{x}, l) = 1 - \frac{\epsilon_l}{\sqrt{\text{Var}(f_l^p(\mathbf{x})) + \epsilon_l^2}} \tag{5-28}$$

$$\alpha_3(\mathbf{x}, l) = \frac{c_1}{c_l}, \tag{5-29}$$

where $\text{cov}(f_1^p(\mathbf{x}), f_l^p(\mathbf{x}))$ denotes the posterior covariance between the high-fidelity process (level 1) and the process at fidelity level l, evaluated at $\mathbf{x}$. The estimated noise levels and computational costs per evaluation at fidelity levels l are denoted by ϵ_l and c_l respectively and they are assumed to be independent of the design parameters $\mathbf{x}$. The noise levels are estimated using maximum likelihood estimation. The optimisation in Eq. 5-26 is performed using a restarted L-BFGS-B method, see [38].

5.4 Mixed-Fidelity ANN

The mixed-fidelity approach uses a combination of low-fidelity computational solution with ANN prediction of high-fidelity information. ANNs are used to model or detect complex nonlinear relationships within systems without using the physics of the system. They are composed of internal parameters to be specified through the process of training. Such parameters are the weights by which the inputs of each neuron are multiplied so that the corresponding output emerges. These weights are tuned so that the error of the output of the ANN (the last layer of neurons) over the available actual data is minimized. The more available actual input and output data the better. This part of the optimization algorithm is critical. The training proceeds by updating the weights in each iteration to conclude with a minimum error.

6 MULTI-FIDELITY OPTIMIZATION FRAMEWORKS

Hull-form parameterization approaches, physical models/solvers, and MF integration methods are combined to form four MF optimization frameworks (see Table 5-3), each investigated by a single institution participating in the AVT-331 Sea Team, as follows.

Framework A developed by CNR-INM, combines the application of PME to the FFD design space with SRBF method, trained by CFDShip-Iowa and WARP (HF and LF solvers, respectively) for the solution of resistance objectives of problems 1 and 2 and CFDShip-Iowa and SMP (HF and LF solvers, respectively) for the evaluation of the seakeeping merit factor of problem 2. Active learning approach (the LCB method) and problem 1 are solved via a memetic single-objective deterministic particle swarm optimization algorithm (DPSO) [39], whereas problem 2 is solved via a multi-objective DPSO [40].

Table 5-3: Multi-fidelity optimization frameworks.

Frameworks	Problems	Design parameterization	Solvers	MF approaches	Team
A	1	FFD/PME	CFDShip-Iowa, WARP	SRBF	CNR-INM
	2	FFD/PME	CFDShip-Iowa, WARP, SMP	SRBF	CNR-INM
B	1	Akima	OpenFOAM, ITU-Dawson	KPLS	ITU
C	1	Blending	ReFRESCO	AIEK	MARIN
D	3	CAESES	MaPFlow, SWAN2, SPP-86	Mixed-ANN	NTUA

Framework B developed by ITU, combines the Akima's surface design with KPLS method, trained by OpenFOAM (HF) and potential flow solver ITU-Dawson (LF) for the solution of resistance objectives of problem 1. A further single-fidelity optimization based on ANN trained by ITU-Dawson is also performed for comparison.

Framework C developed by MARIN, combines the blending approach for the design design parameterization, along with the Augmented Expected Improvement-based Kriging (AEIK) method, trained by ReFRESCO (HF and LF changing the computational grid) for the solution of resistance objectives of problem 1.

Framework D developed by NTUA, combines the parametric design space based on CAESES with a mixed-fidelity approach that includes ANN for the solution of problems 1 and 3. Specifically, the resistance objective is based on SWAN2 as basis for LF fidelity computation and SPP-86 for the seakeeping performance. The optimization is conducted with NSGA-II [41] in a surrogate-free fashion, using the ANN only to correct the LF estimate of friction resistance component.

7 RESULTS

The results obtained using the MF frameworks of Table 5-3 are provided and discussed in the following subsections.

7.1 Framework A

URANS (CFDShip-Iowa) computations are used to evaluate both calm-water and seakeeping performance. The latter are achieved starting form the calm-water results. The computational domain is composed by a background (3.5M points) and a boundary layer ($\sim$1M points) volume grids, taking advantage of problem symmetry. The boundary layer volume grid is designed to have $y^+ < 1$, avoiding the use of wall functions. A detail of the computational grid is shown in Fig. 5-4 (left). Potential flow (WARP) is used to evaluate calm-water resistance that is used as LF-level for both calm-water and seakeeping problem. The computational domain is composed

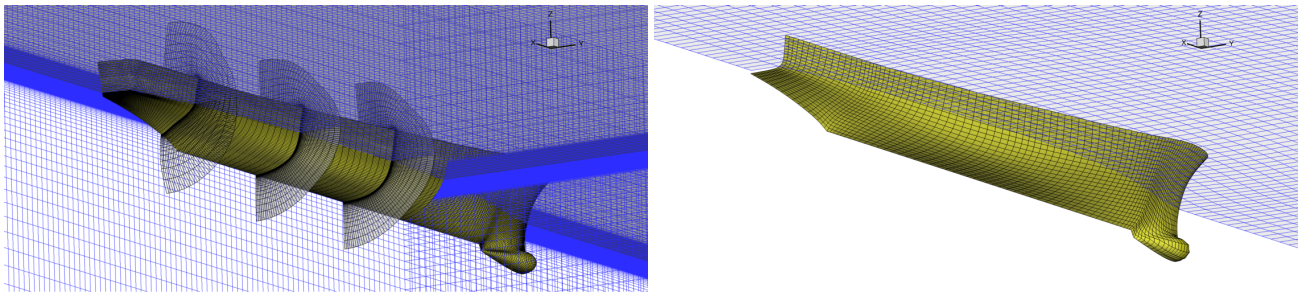

Figure 5-4: Computational grids for HF (left, CFDShip-Iowa, RANS) and LF (right, WARP, potential flow) solvers (framework A).

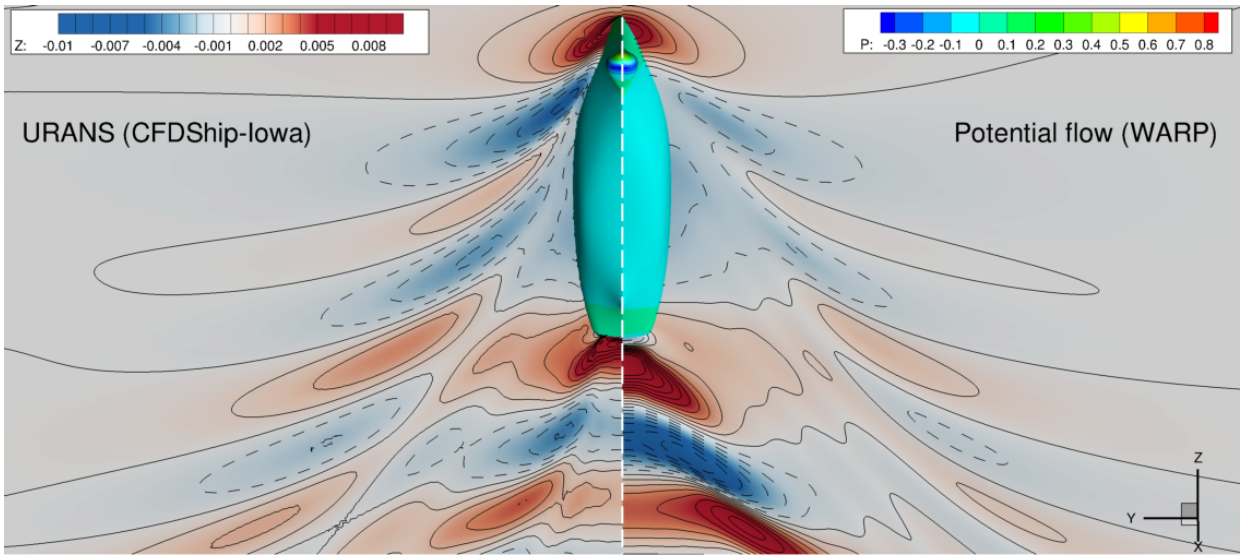

Figure 5-5: Comparison of URANS (left) and PF (right) wave elevation pattern and pressure field along the original hull (framework A).

by the free-surface (7.6k points) and the hull (9k points) surface grids, taking advantage of problem symmetry. A detail of the computational grid is shown in Fig. 5-4 (right).

Comparison of HF and LF pressure fields and wave elevation patterns for the original hull are shown in Fig. 5-5. Pressure distributions are in a reasonable agreement, whereas the wave elevation obtained by potential-flow presents under-predicted diverging bow waves and over-predicted diverging stern waves. Although the overall agreement is quite promising for application in the MF context, the limitation of PF solvers stems from their inability to properly identify performance losses associated to flow separations that might occur in some regions of the design space. This poses a methodological challenges for their use in the MF framework.

For seakeeping conditions, motions response to the encounter wave determines the second objective function in Eq. 5-3. Computational domain and grids used for the assessment of seakeeping performance by the URANS solver are the same used for the evaluation of calm-water resistance. It may be noted that the background grid has been defined to discretize both wave length and height with 100 grid points, will computational time discretization is defined to have one encounter wave period with 256 time steps. Linearized strip theory potential

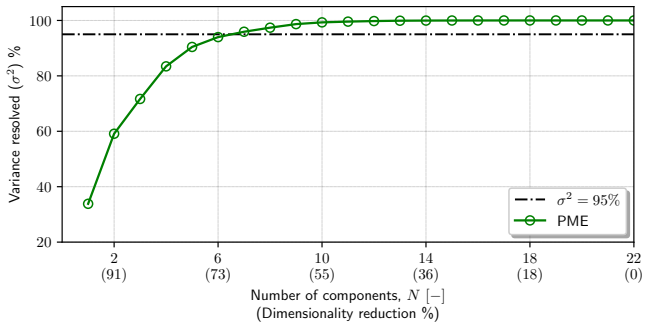

Figure 5-6: Design-space dimensionality reducion results via PME (framework A).

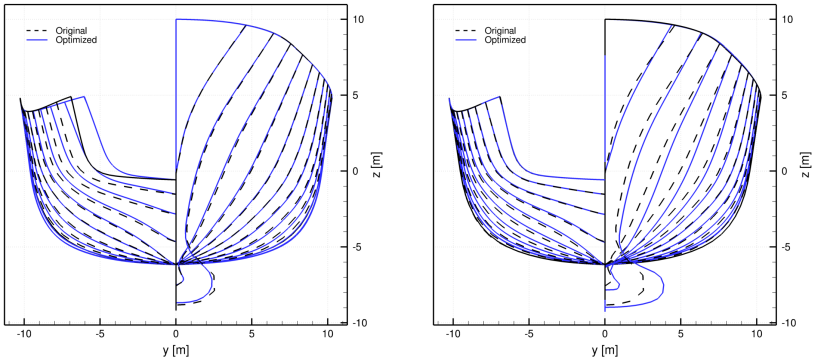

Figure 5-7: Comparison of original and the optimized hull stations (framework A).

flow simulations by SMP are performed taking advantage of hull symmetry. The hull is discretized with 31 strips and each of them is discretized with 10 nodes equally spaced along the strip curvilinear coordinate. Solvers verification and validation can be found in [7]. The computation cost ratio between HF and LF solvers is equal to 0.001.

Since surrogate-models suffer the curse of dimensionality, so their training can be quite expensive with high-dimensionality problems, the original FFD ($M = 22$ design parameters) is reduced in dimensionality trough a parametric model embedding (PME) approach [8]. The method is simulation-free and allows to reduce the dimensionality of the design space, retaining at least a prescribed level of the geometrical variance of the original design space. The method is fed by a bunch of hull variants and the associated design parameters and provide a reduced order model of the original design parameterization, allowing its direct reconstruction. For further details, the interest reader can refer to Serani and Diez [8]. Specifically, PME is trained by 1000 Monte Carlo realizations of the design space (each realization is a modified hull shape and the associated design

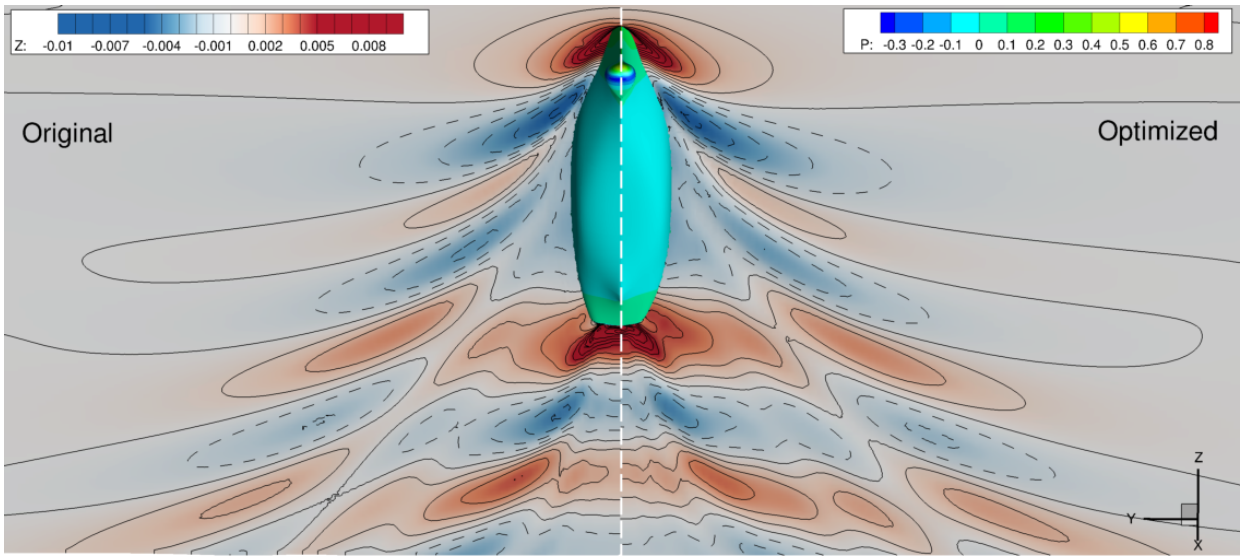

Figure 5-8: Comparison of original and the optimized wave elevation pattern and pressure field along the hull (framework A).

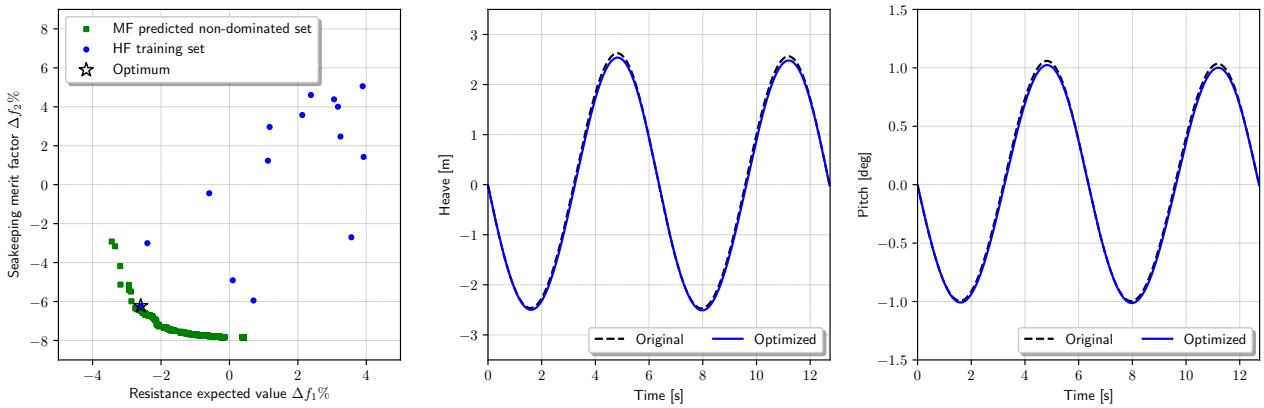

Figure 5-9: Problem 2 non-dominated solution set (left) and comparison of heave (center) and pitch (right) motions for the original and the optimized hulls (framework A).

parameters) achieving a dimensionality reduction of almost 70% ($N = 7$), retaining at least the 95% of the original geometrical variance. The cumulative sum of the variance resoved as a function of the PME reduced design variables is shown in Fig. 5-6.

MF surrogate model begin with an initial training set composed by a face-centered central composite design (CCF) for the LF level, corresponding to 15 training point, and only 1 HF training point in the domain center. Optimization is stop when 15 high-fidelity samples are added to the training set. Optima for both problem 1 and 2 are achieved training the MF-SRBF method with 15 HF and 647 LF evaluations, providing 5.8% resistance reduction in calm-water for problem 1 and 2.6% expected resistance reduction with 6.2% SMF improvement in regular waves for problem 2. Both achievements are quite significant, specially the second, since in previous activity (AVT-252) no compromise solution capable of improving both resistance and seakeeping objective have been found. Nevertheless, problem 1 and problem 2 optima are quite different and their comparison with the original hull stations is shown in Fig. 5-7. Specifically it can be seen how calm-water (problem 1) optimum has basically not changed the forward part of the vessel, whereas a significant restriction of stern region is achieved. This latter results affects both pressure and wave elevation fields as shown in Fig. 5-5. Specifically,

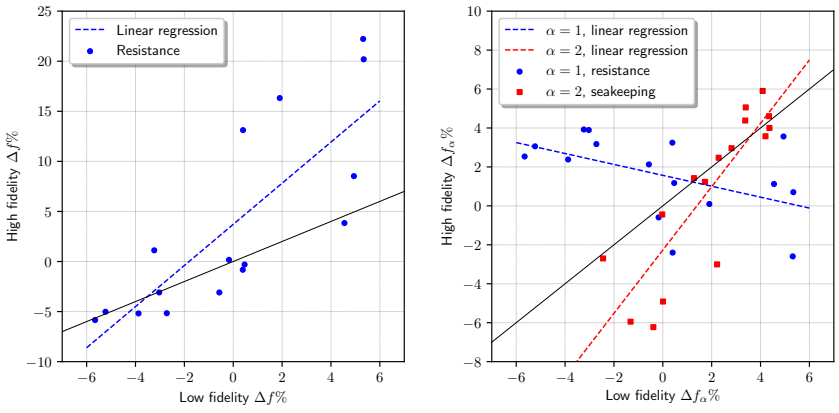

Figure 5-10: Objective functions correlation for HF and LF numerical solutions (framework A).

the optimized hull provides a better recovery of the pressure towards the stern, as well as a mild reduction of the diverging stern waves. For what concerns problem 2, the shape modification is quite is opposition with the calm-water problem; specifically, the optimized vessel has larger stations towards the forward perpendicular, with a significant modification of the bow dome, while no significant differences are visible towards the aft perpendicular. Problem 2 optimal hull has been selected as the best trade-off solution on the MF-predicted non-dominated solution set, as shown in Fig. 5-9, left), where HF training points and optimum validation are also shown. Furthermore, Fig. 5-9 (center and left) provides a comparison of heave and pitch motions with the original vessel. Since, compared to the original hull, a very low reduction of heave and pitch response at the center of gravity is achieved, the enlargement of the bow dome has had, as main effect, the breaking of the head waves, allowing for the resistance reduction expected value. This last achievement deserves for further future investigation.

One last analysis of the MF-based optimization outcomes has been conducted on the correlation of the information sources. Specifically Fig. 5-10 (problem 1 on the left and problem on the right) provides the objective functions relative variation of the LF vs HF training points. Problem 1, in calm-water (see Fig. 5-10, left) shows a quite good correlation (see the linear regression line) between the two information sources, even if not perfect (represented by the black line), meaning that, for this specific problem, the potential flow can be quite effective (probably when no separation phenomena occurs), but at the same time can provide huge under/overestimation of the objective function variation, probably due to separation phenomena, that cannot be modelled. Problem 2 results (see Fig. 5-10, left) provide several food for thought: (1) seakeeping performance are in good correlation, showing how, at least for the current application, the strip theory is quite effective, compared to URANS, with some hints of underestimation of the objective function; (2) contrary to problem 1, here potential flow, that not take into account for the added resistance, and URANS solutions tend to be in anti-correlation, this means that between the two information source there is a quite non-linear relationship (harder to be modeled by the surrogate model) and that the added resistance component has the highest relevance for the seakeeping problem.

7.2 Framework B

OpenFOAM computational domain is determined by following the ITTC guidelines, thus inlet, bottom, and side boundaries are fixed as $2L_{\mathrm{pp}}$ from the ship model and the outlet boundary is placed $3L_{\mathrm{pp}}$ downstream direction in order to minimize the effect of wave reflection from boundaries of the numerical domain. Boundary conditions are assigned by using ITTC guidelines: lateral sides and bottom boundaries were assigned as symmetry plane; inlet, outlet and atmosphere boundary conditions are determined associated with the turbulence parameters and flow characteristics and wall type boundary condition is adopted for hull surface. Mesh generation is adopted by using BlockMesh utility in OpenFOAM. In order to refine the mesh so as to be close to the hull surface, TopoSet utility is applied for enhancing the mesh density. Two control volumes are modeled around the hull form to resolve the flow characteristics, then snappyHexMesh is implemented to conclude 3D mesh generation process. In scope of this study, different mesh densities are examined as presented in Table 5-4. According to the results, $\sim 2M$ mesh is assigned as HF (entitled as Case-3 in Table 5-4) to be used in MF surrogate model. The variation of mesh densities on the hull surface is depicted in Fig. 5-11, pressure distribution and wave elevations in Figs. 5-12 and 5-13, respectively.

For potential flow solutions, which are employed for LF data, convergence or sensitivity analysis was not presently made for this study, since the mesh convergence studies have been performed on the code ITU-Dawson

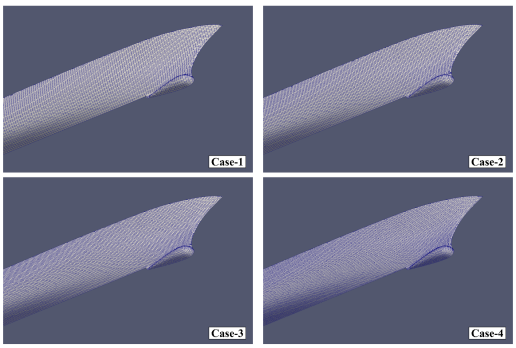

Figure 5-11: Mesh density variation on hull surface (framework B).

Table 5-4: Computational elapsed time* comparison (framework B).

Case	Mesh size	R_T [N]	Elapsed time [hours]
1	0.75M	44.6985	02:38:33
2	1.27M	44.6285	03:02:44
3	2.08M	43.9776	03:11:47
4	3.75M	43.6124	10:11:21

* Processor: Intel Xeon E5-2680 v4, 28 cores.
(The ITU - National High Performance Computing Application and Research Center)

for similar hull forms. The latest grid convergence study regarding with ITU-Dawson can be seen in Goren et al. [42]. Based on the previous experience, 1.8k panels over the hull surface (demi-hull) and 2k panels over the free surface (half symmetric plane) are distributed, Fig. 5-14 (left). As a validation attempt, a comparison of wave resistance coefficients obtained by ITU-Dawson with those of the experimental data is presented in Fig. 5-14 (right).

In this study, in order to deeply and more systematically investigate the performance of the MF–KPLS method, i) the number of PLS components are taken as 3 (MF–KPLS3) and 4 (MF–KPLS4) and ii) the number of the data associated with different fidelities are selected as diverse combinations. A Design of Experiments (DoE) is given in Fig. 5-15 with total resistances of 1000 modified hull forms obtained by means of Low–Fidelity (LF) computations. Fig. 5-16, on the other hand, gives an idea on how the present hull form modification approach fills the space (by taking only the points 1, 5, 10 and 15 out of 18 control points). To give an idea about the correlation between HF and LF, a limited number of LF and corresponding HF results are presented in Fig. 5-17.

To assess prediction performance of the surrogate model, two global accuracy metrics are used: coefficient of

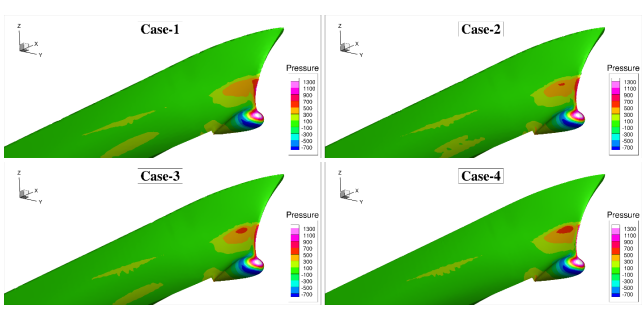

Figure 5-12: Pressure distribution on the hull surface (framework B).

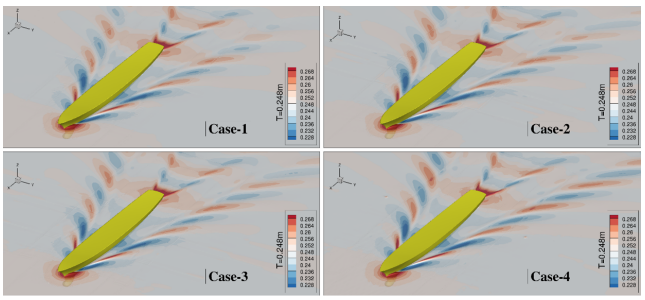

Figure 5-13: Wave elevation around the hull form according to different mesh density (framework B).

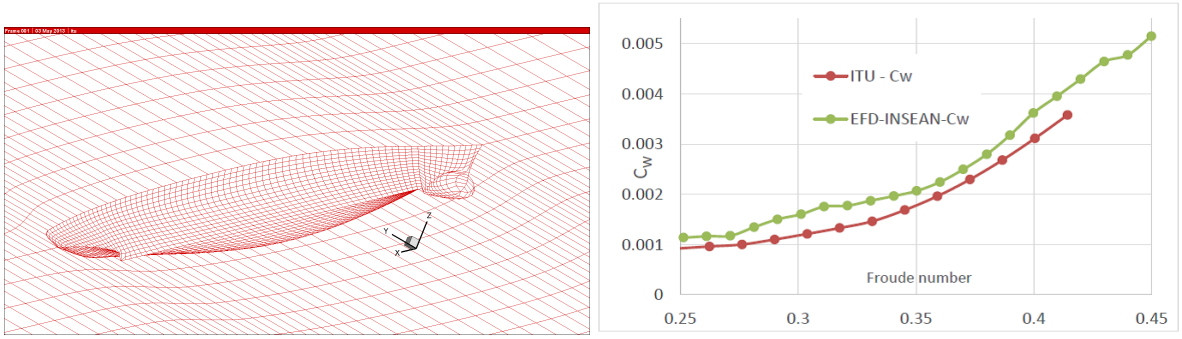

Figure 5-14: Panel distribution over the parent hull and its free surface vicinity (left) and computational wave resistance coefficient as compared with EFD (INSEAN) data (right), within framework B.

determination (R^2) and root-mean square error (RMSE) defined as in the following, respectively.

$$R^2 = 1 - \frac{\sum_{i=1}^{N} (y_i - \widehat{y}_i)^2}{\sum_{i}^{N} (y_i - \bar{y})^2}, \quad \text{RMSE} = \sqrt{\frac{1}{N} \sum_{i=1}^{N} (y_i - \widehat{y}_i)^2} \tag{5-30}$$

Surrogate model performance assessments are presented in Table 5-5, where 30 HF test data are used to determine the error metrics. Global error metrics are presented as their normalized values. Normally, it is expected that, as the number of data increases in one or in both of the fidelities, the R^2 should be increased -ideally reaches to 1, which means surrogate model produces accurate/exact predictions- and RMSE decreases. Nevertheless, when Table 5-5 is examined, it can be concluded that this is not the case. One may deduce from Table 5-5, as well, that for some specific combinations the MF surrogate modeling results in high correlation and

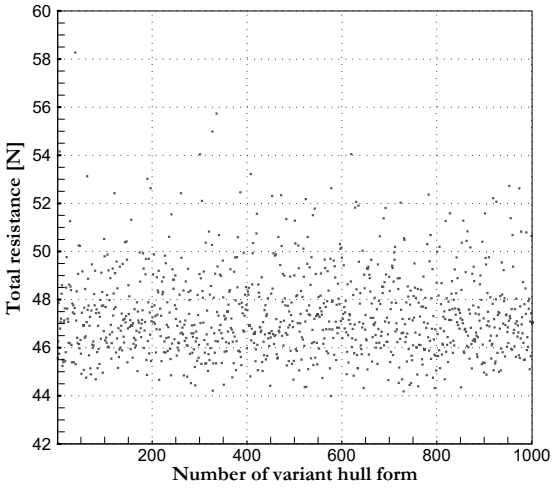

Figure 5-15: Set of DoE for LF within framework B.

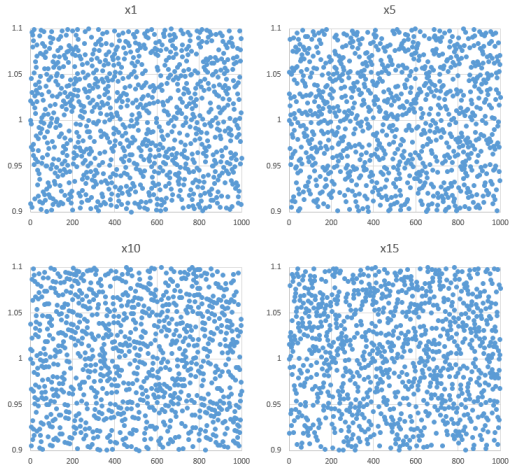

Figure 5-16: Control points (1, 5, 10 and 15) of the modified hull forms showing their distribution in the space limited to $\pm 10\%$ of the original offsets within framework B.

highly reduced RMSEs. Although it may be misleading to derive solid conclusions from Table 5-5; relatively higher number of HF data seems not to be helpful to increase the performance of MF surrogate modeling. It may also be said that Table 5-5 shows also the limits of static sampling strategy and inherent uncertainties in it.

The results of the present optimization study based on an MF strategy are summarized in Table 5-6. All the surrogate modeling attempts given in Table 5-5 are utilized in the optimization process to observe their usefulness. Here, error of the surrogate model $\Delta\%E$, represents the difference between the surrogate prediction and the HF simulation. In addition, the resistance gain according to parent hull is presented in the last column, $\Delta\%R$, and $-\Delta\%R$ values stands for relative gain with respect to parent hull in total resistance. In this table, every row corresponds to different combinations of HF and LF data (in Table 5-5) and all surrogate model implementations were utilized in the optimization process by using SciPy's differential evaluation tool [43] which is widely used stochastic population based method for global optimization problems.

As seen in Table 5-6, the best attempt for MF–KPLS3 and MF–KPLS4 methods (accomplish 5.13 % and 5.72 % reductions, respectively) use same combination of fidelity data as 1000 LF and 20 HF, which has the best performance in surrogate modeling in terms of error metrics according to Table 5-5. Meantime, ITU treats single–fidelity (SF based on potential flow solver ITU–Dawson) surrogate modeling by ANN with the same number of design parameters (18) and arrives at 4% reduction in total resistance with respect to parent hull – as confirmed by HF solver – which points out that a proper MF surrogate modeling could be more effective in the hull form optimization. The best optimum hull form for (MF–KPLS) method and single–fidelity ANN (SF–ANN) are compared in Fig. 5-18. Performance of the optimal hull form as compared with that of original (parent) hull form in terms of wave elevations and pressure distribution on the hull surface can be observed in Fig. 5-20.

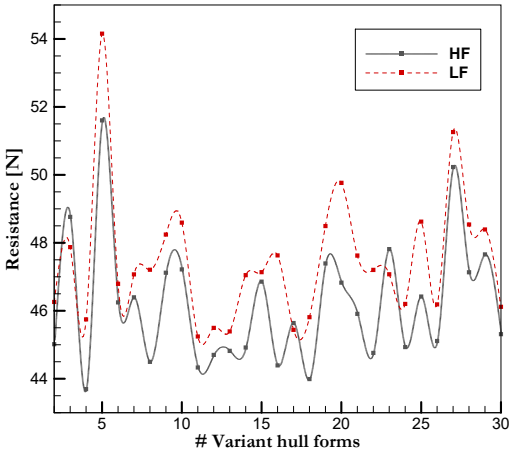

Figure 5-17: Comparison of LF and HF results of total resistance within framework B.

Table 5-5: Performance assessment of MF–KPLS within framework B.

		MF–KPLS3		MF–KPLS4	
LF	HF	*R2	*RMSE	*R2	*RMSE
1000	15	0.650	0.310	0.686	0.114
1000	20	1.000	0.000	1.000	0.000
1000	30	0.702	0.261	0.738	0.094
1000	40	0.072	0.913	0.106	0.361
1000	60	0.000	1.000	0.000	0.414
250	60	0.000	1.000	0.000	0.414
350	60	0.000	1.000	0.000	0.414
500	60	0.000	1.000	0.000	0.413
700	60	0.000	1.000	0.001	0.413
1000	60	0.000	1.000	0.000	0.414
250	15	0.647	0.313	0.683	0.115
350	20	0.663	0.298	0.698	0.109
500	30	0.703	0.261	0.738	0.094
700	40	0.072	0.913	0.106	0.361
1000	60	0.000	1.000	0.000	0.414

$*$ Represents normalized values within the range.

Table 5-6: Prediction evaluation of MF–KLPS with framework B – as the result of optimization.

LF	HF	MF–KPLS3 [N]	CFD [N]	$\Delta\%E^{\dagger}$	$\Delta\%R^{\ddagger}$	MF–KPLS4 [N]	CFD [N]	$\Delta\%E$	$\Delta\%R$
1000	15	39.379	43.122	-8.68	-1.95	39.372	42.774	-7.95	-2.74
1000	20	40.485	41.721	-2.96	**-5.13**	40.086	41.463	-3.32	**-5.72**
1000	30	40.499	42.190	-4.01	-4.07	40.496	42.259	-4.17	-3.91
1000	40	44.135	46.443	-4.97	5.61	44.124	42.259	4.41	-3.91
1000	60	44.135	43.550	1.35	-0.97	43.438	43.131	0.71	-1.92
250	60	43.887	45.398	-3.33	3.23	44.268	45.133	-1.92	2.63
350	60	44.001	44.832	-1.85	1.94	44.262	45.176	-2.02	2.73
500	60	44.127	44.626	-1.12	1.47	44.161	45.393	-2.71	3.22
700	60	44.124	43.808	0.72	-0.39	44.317	44.254	0.14	0.63
1000	60	44.288	43.718	1.30	-0.59	44.311	46.618	-4.95	6.00
250	15	38.823	44.022	-11.81	0.10	38.805	43.926	-11.66	-0.12
350	20	39.821	42.574	-6.47	-3.19	39.792	42.719	-6.85	-2.86
500	30	40.508	43.487	-6.85	-1.12	40.506	43.424	-6.72	-1.26
700	40	44.160	43.975	0.42	-0.01	44.066	44.909	-1.88	2.12
1000	60	44.289	43.279	2.33	-1.59	44.311	46.735	-5.19	6.27

† Prediction error of the metamodel according to CFD; ‡ The percentage of Resistance gain relative to parent hull.

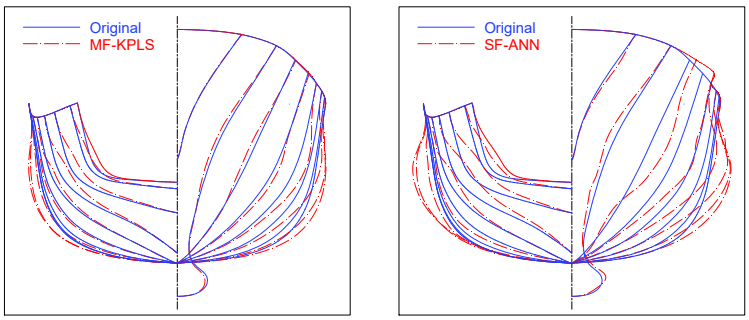

Figure 5-18: Geometrical comparison of optimal hull forms with parent hull (left:MF-KPLS, right:SF-ANN) for framework B.

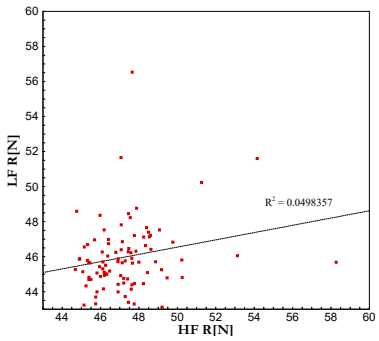

Figure 5-19: Correlation between LF and HF simulations for framework B.

The rest of the constructed surrogates, especially in some cases, are pretty far to be regarded as optimum. Therefore, a number of issues can be discussed for the sake of MF strategy. In this study, maximum 60 HF simulations are used to train the surrogate model and 30 HF simulations are used to assess the surrogate model global accuracy. In Figure 5-19; total HF simulations (60) are presented to visualise the correlation with their counterpart LF simulations. According to this figure, the discrepancy between LF and HF simulations is excessive, making the implementation of MF strategies challenging. Another issue that has to be considered is the amount of data used to train the surrogate model according to the dimension of the problem. For such a high-dimensional SBDO problem, dimension reduction strategies should be examined to maintain the advantage of MF implementation, so as to keep required number of training HF data as small as possible. Initially, ITU implemented Co-Kriging surrogate modeling to the offline DoE set and it was then observed that the surrogate

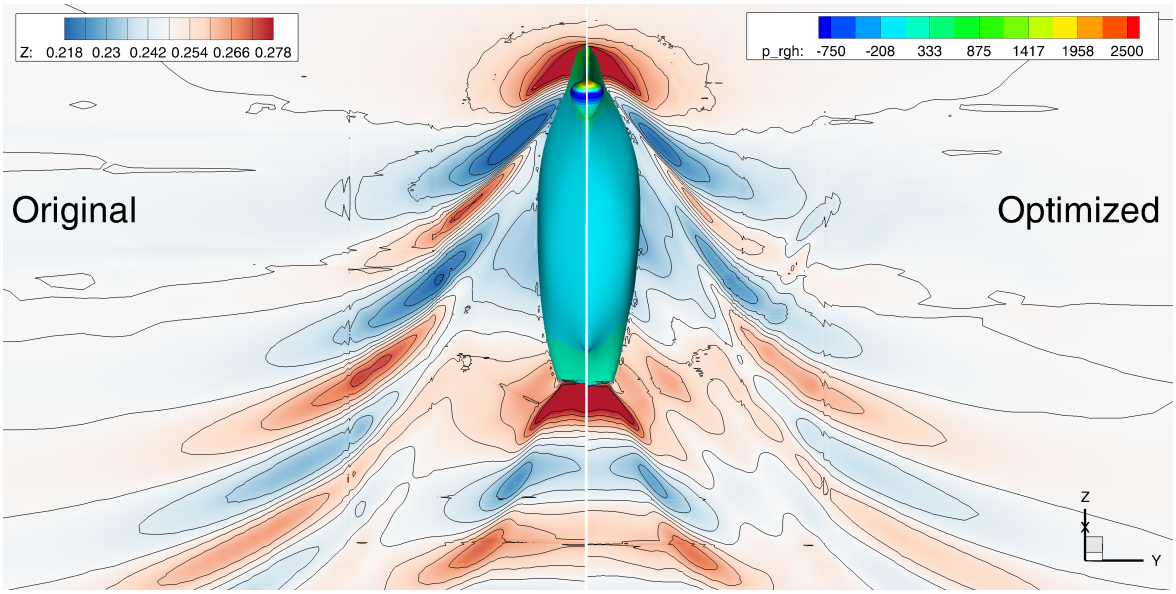

Figure 5-20: Comparison of wave elevations on the free surface and pressure distribution on the hull surface of the original (parent) and the optimized hull forms (framework B).

model cannot provide adequate resistance reduction. The underlying reason may be both the lack of enough data to train the surrogate model which is strongly related with the dimension of the problem and may be due to the level of noise in the data set. In order to solve the problem encountered; instead of directly considering the noise level in DoE, ITU applied KPLS to overcome the bottlenecks, which may be related with the lack of data and/or noise in the data set. According to the results, the KPLS is able to attain significant reductions in total resistance for the same DoE in the optimization process. This may be attributed to the fact that KPLS is able to take into account of important and sensitive dimensions in the design space. In addition, regarding the results presented in Table 5-5 and Table 5-6, especially in some cases, increasing the training data results in decreased surrogate model accuracy which probably means that new points are added as training samples from unresolved/unexplored regions and accordingly the accuracy of the model is decreased. Alternatively, to enhance the surrogate model strategy, adaptive sampling strategy may also be considered to prevent additional computational cost associated with sampling the unnecessary regions.

7.3 Framework C

For the solution of problem 1, the LF grid consists of approximately 1.7M cells, whereas the HF grid consists of approximately 15M cells, see Figure 5-21. The computational cost for the low-fidelity solution takes approximately 22 minutes using 240 cores on 10 nodes where each node has 2 Intel(R) Xeon(R) Gold 6126 CPU @ 2.60 Hz 12 core CPUs. Using the same resources, the high-fidelity computation takes about 165 minutes to complete (note that the computational cost includes the grid generation process). This reflects in a computational cost ratio equal to $c_2/c_1 = 0.13$. A CCF design of experiments is used for both the initial high- and low-fidelity sampling plans. The rationale behind this choice is that it provides a relatively coarse initial sampling plan, leaving more budget for the adaptive phase of the optimization method. A budget of 10 is given to the optimization procedure.

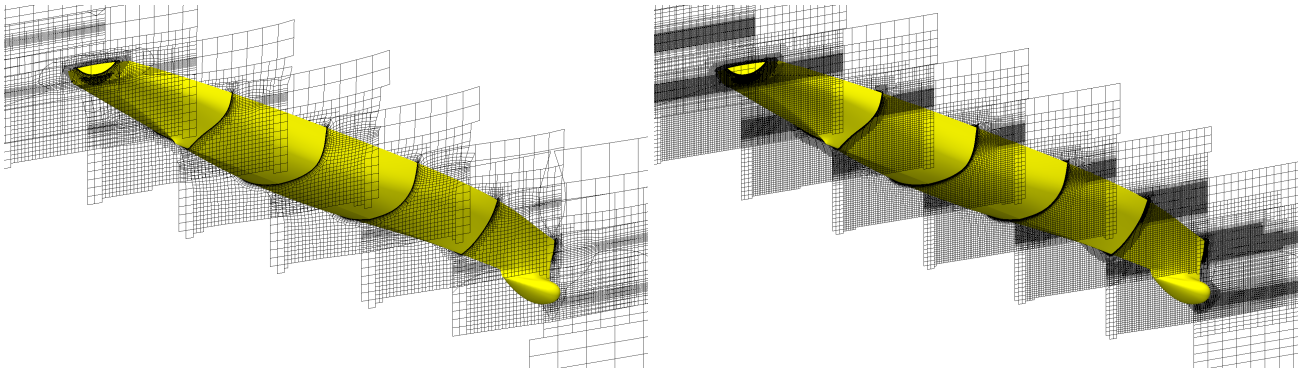

Figure 5-21: Visualisation of the LF (left) and HF (right) grids for ReFRESCO (framework C).

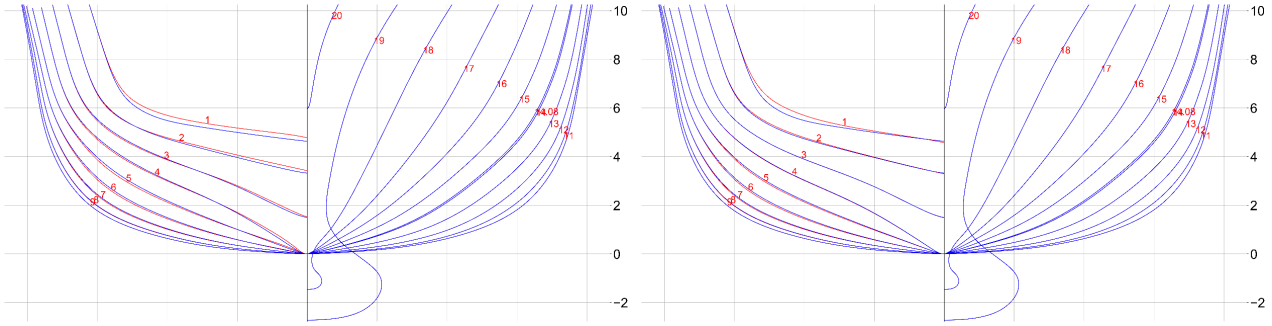

(a) Single-fidelity *(b) Multi-fidelity*

Figure 5-22: Visualisation of the LF (left) and HF (right) grids for ReFRESCO (framework C).

The optimization results are collected in Table 5-7, where N denotes the dimensions of the design space, L the fidelity levels used, CC the computational budget, $\mathcal{J}$ the number of evaluations, $f_1(\mathbf{x}^*)$ the resistance value at the optimum design $\mathbf{x}^*$, ϵ the estimated noise level and x_i^* the i^th element of the vector $\mathbf{x}^*$. The original hull has a full scale resistance of 43.06 N, where 31.21 N is due to friction and 11.84 N is due to pressure. The AEIK method finds a slightly better design. A total resistance reduction is obtained of about 1.05% using the multi-fidelity method whereas the single-fidelity counterpart obtains 0.93%. The reduction of the pressure resistance is 3.72% and 3.21% respectively, while no significant reduction of the frictional resistance is observed. During the initial exploration phase of the multi-fidelity optimization method, the algorithm decides to trade 2 HF evaluations for 18 LF evaluations (resulting in a final budget of 10.42).

The optimal hull shapes corresponding to Table 5-7 are shown in Figure 5-22. The optimal hull shapes are very similar but differ in the amount of V-shape applied to the aft-ship.

Table 5-7: SDDO Results for Framework C.

Case	N	L	CC	$\Delta_x\%$	$\Delta_f\%$	$\mathcal{J}$	$f_1(\mathbf{x}^*)$ $[N]$	Fric. [N]	Press. [N]	ϵ $[N]$	x_1^*	x_2^*	x_3^*
Original hull	-	-	-	0.00	0.00	-	43.06	31.21	11.84	-	0.000	0.000	0.000
Single-fidelity	3	1	10	65.82	-0.93	10	42.66	31.20	11.46	4.73E-7	0.266	1.000	0.478
Multi-fidelity	3	1-2	10	75.83	-1.05	8-18	42.61	31.20	11.40	4.90E-3	0.000	1.000	0.852

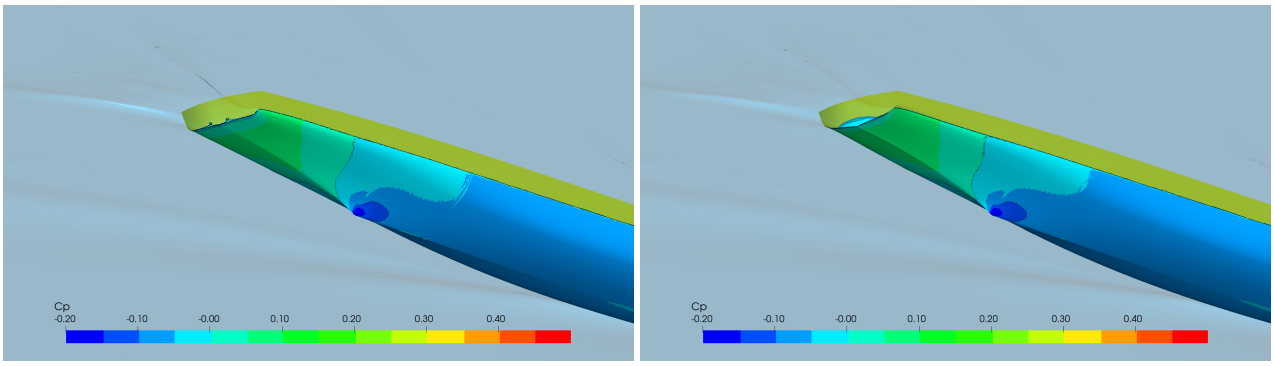

(a) Original hull *(b) Optimized hull*

Figure 5-23: Pressure around the 5415 hull, before and after the optimization with framework C.

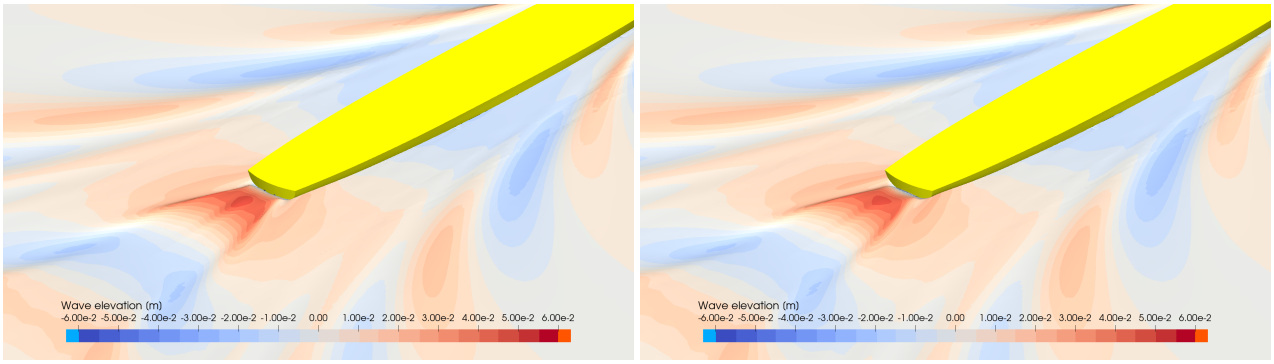

(a) Original hull *(b) Optimized hull*

Figure 5-24: Stern wave from the 5415 hull, before and after the optimization with framework C.

Figure 5-23 shows the pressure coefficient on the 5415 hull, before and after the optimization with the multi-fidelity method. It can be seen that the optimized hull has a better pressure recovery than the original hull. This results in a reduced pressure resistance and a small increase in the dynamic trim with 0.01 deg, bow down.

The stern wave system is shown in Figure 5-24. The stern waves from the optimized hull are slightly less pronounced than the stern waves from the original hull.

7.4 Framework D

The panel mesh generation of the free-surface and the body surface of the hull is an internal routine of SWAN2 2002. The spline sheet of the body surface is defined by 45 nodes in a direction parallel to the x-axis, corresponding to 44 panels along the hull and by 13 nodes on each lateral section. The domain of the free surface accounted in the calculations extends $0.5L_{\mathrm{pp}}$ upstream, $1.5L_{\mathrm{pp}}$ downstream, and $1.0L_{\mathrm{pp}}$ in the transverse distance (athwartships). Figure 5-25 presents the spline sheet of the free-surface (left) and the body (right).

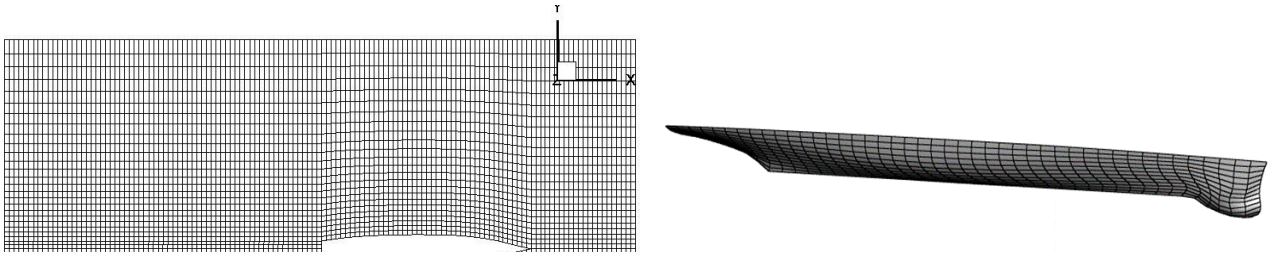

Figure 5-25: Spline sheet on the computational grid of SWAN2 (framework D).

A relatively low number of data available to train the ANN has been used. Specifically, the ANN is trained with only 27 examples as input, which correspond to the 27 combinations of three values per variable, the two selected limiting ones, and the value of the parent hull for the three chosen stern geometrical variables affecting the optimization scheme. Usually, the stern design variables are two to four and three values per variable are sufficient to train a reliable ANN, since the variation of the variables is limited. The use of limited CFD calculations is a major advantage of the proposed methodology. The derived ANN is handled by a genetic algorithm, which, after 400 evaluations, reaches the optimum combination of the stern variables. Selection of a suitable ANN structure is probably the hardest part of the problem and critical to obtaining accurate predictions. Since dealing with a regression problem, the multilayer perceptron (MLP) concept was applied consisting of an input, hidden, and output layer, as well as utilizing a back-propagation learning algorithm. The development of the ANN was performed in Python assisted by the Tensorflow/Keras neural network library. The usual search process for the optimal neural network goes through the following steps: data normalization, division of data set, selection of ANN model architecture, and finally the assessment of ANN model results. In this study, the small number of available training data significantly hindered this process. Input data were normalized using a custom Min/Max scalar function centered around parent hull resistance value with a 20% reserve. This reserve was used to ease the first step of optimization process, ANN's function minimization search, by allowing us to extrapolate values beyond observed ranges. Moreover, during ANN model's training, no validation set was used. It was decided to use every data point available for the more efficient training of the network and take the risk to validate the model's prediction at the final stage of optimization procedure via CFD calculations. Trials with different configurations were conducted to identify the ANN architecture that is better suited to the problem. The number of input neurons was set to three, representing the three variables set at the vessel stern region, and the

Table 5-8: Overview of the best ANN performance for framework D.

Code	Input layer	Hidden layer(s)*	Output layers	MSE	MAE
N-1	3	6(S)–4(S)	1(S)	2.1E-3	3.3E-2
N-2	3	6(S)	1(S)	4.3E-2	1.7E-1
N-3	3	6(S)–3(R)	1(S)	4.4E-2	1.7E-1
N-4	3	6(S)–3(R)–3(R)	1(S)	4.0E-2	1.6E-1
N-5	3	12(S)	1(S)	4.6E-2	1.9E-1

*Activation functions: R – ReLU (Rectified Linear UNit), S – Signmoid

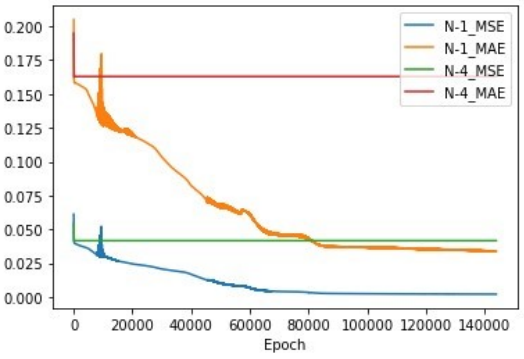

Figure 5-26: MSE and MAE convergence during the ANN training process (framework D).

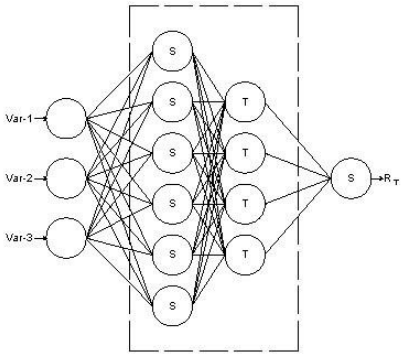

Figure 5-27: Architecture of the selected ANN model (framework D).

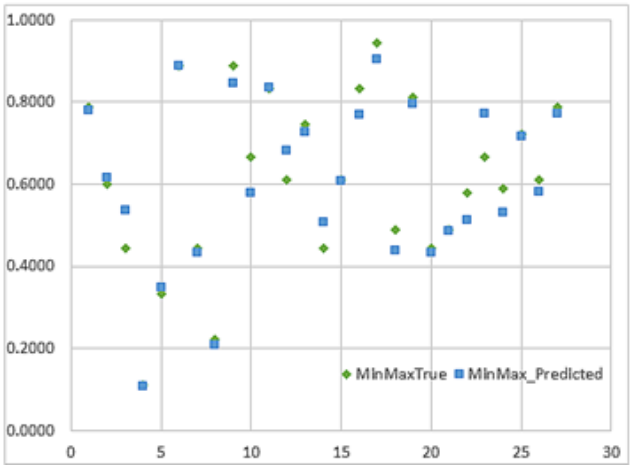

Figure 5-28: ANN input vs. predicted values (framework D).

output node was set to one referring to the target value of CFD calculation. The rest of the ANN configuration as determined by the number of hidden layers, the number and type of neurons that comprise each one of them, the training algorithm, learning rate, and the backpropagation optimizer method went through exhaustive numerical experiments, probably an inevitable stage when developing an . An overview of the performance of the best ANN models is presented in Table 5-8. The number of neurons at each layer and their activation functions can also be seen.

The mean squared error (MSE) function was used as the loss or cost function under minimization during models' training. Notice should be kept, though, on the mean absolute error (MAE) as well. The progression of MSE and MAE values during training is presented in Fig. 5-26. The network (N-1) that showed the lowest MSE and MAE error was selected in order to evaluate hull surrogate-models. It consists of the three stern parameters as inputs,

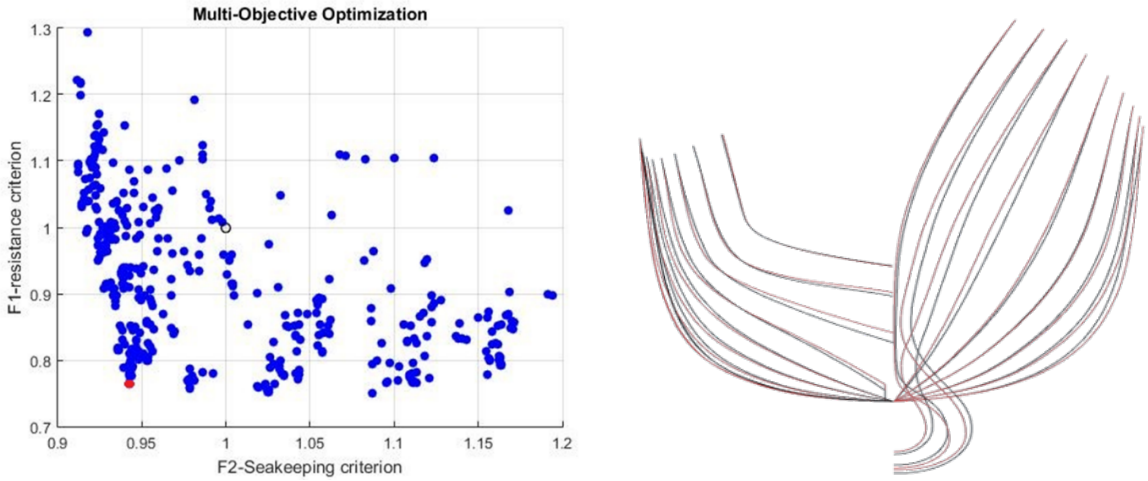

Figure 5-29: Hull variants of the multi-objective optimization (left) and comparison of the body plans (right) of the optimized (red) and parent (black) hulls (framework D).

two hidden layers comprised of six and four nodes, respectively, and the output layer. To overcome the problem of vanishing gradients and saddle points, the sigmoid function was used as an activation function at input, first, and output layer of the network, while hyperbolic tangent was utilized at the second layer. Stochastic gradient descent with momentum was selected against ADAM as the back-propagation optimizer method, learning rate, and momentum were set to 0.16 and 0.7, respectively. Selected ANN model's architecture and performance are presented at Figs 5-27 and 5-28. The Pearson coefficient was calculated at 0.975. The small size of the training data led to an increase of epochs performed in order to get satisfactory results. For the best configuration found, the number of epochs was set at the scale of 150k. Despite the large number of epochs, the training procedure required less than 5 min to complete at an i7 9700K.

The results of the multi-objective optimization problem 3 are shown in Fig. 5-29. Following a preliminary generation of variant hull forms by varying progressively only one of the design variables at a time, the feasible range of the design geometrical were roughly specified. A few of the derived variants are aborted by the evaluation algorithms since they don't constitute feasible designs.

A standard evolutionary algorithm, the Non-dominating Sorting Genetic Algorithm-II (NSGA-II) was used to drive the optimization scheme. A total of 400 variants of the parent hull form were generated by CAESES software. The variant hull forms, the selected optimal one (red) and the parent hull form (white) are all depicted in Fig 5-29 (left). Figure 5-29 (right) shows the body plans of the parent hull form compared with the optimum one, that achieves about 23% of reduction for the weighted resistance function and 5.8% seakeeping performance improvement.

8 CONCLUSIONS

The paper presented and discussed the efforts by the AVT-331 Sea Team in solving the L3 sea benchmark problems for the resistance and seakeeping optimization of a destroyer-type vessel, namely the DTMB 5415 model. Several multi-fidelity approaches were presented and discussed, with application to three design (global) optimization problems of the same vessel. Specifically, the design optimization problems aimed at: (1) minimization of the total resistance in calm-water at $\mathrm{Fr} = 0.28$ (model scale); (2) minimization of the expected value of the total resistance in regular head waves and maximization of the seakeeping performance at $\mathrm{Fr} = 0.28$; and (3) minimization of the total resistance in calm-water and maximization of the seakeeping performance in waves at $\mathrm{Fr} = 0.25$ and 0.41.

Different hull-form parameterization methods were presented and applied, based on free-form deformation, Akima's surface generation, hull blending, and CAD parametric modeling. Furthermore, a dimensionality reduction procedure via parametric model embedding was used to obtain a reduced-dimensionality representation of high-dimensional design spaces, introducing a multi-fidelity approach in the hull-form representation. Physical models and numerical solvers include unsteady Reynolds-averaged Navier-Stokes, potential flow, and strip theory methods. Different solvers and spatial discretizations were used as different information source in multi-fidelity optimization. Different multi-fidelity integration approaches were shown and discussed, exploring static and dynamic surrogate models, as well as mixed approaches. As surrogate model, stochastic radial basis functions, Kriging, Kriging with partial least squares, and artificial neural networks were investigated. Multi-fidelity versions of the lower confidence bounding and augmented expected improvement were used for the active learning process (adaptive sampling) of surrogate models. Finally, four computational multi-fidelity frameworks (A, B, C, D) were individually applied by the AVT-331 Sea

Team members, combining different physical models/solvers, hull-form parameterization approaches, and multi-fidelity integration methods, and finally applied to different design (global) optimization problems.

The present effort highlighted how the dimensionality of the optimization problem (i.e., the design space dimensionality) may be a critical issue for the (global) surrogate model training, which is certainly true also and especially if only high-fidelity evaluations are used. In the present context, **the proposed multi-fidelity approaches were able to achieve significant objective-function improvements, even if only a few high-fidelity evaluations were used, which is one of the most valuable outcomes of the present collaborative research effort. Specifically, the ratio between the number of high- and low-fidelity evaluations required to solve the global optimization problem was found as low as nearly 1/50.** Furthermore, a viable option for improving the training process by overcoming the curse of dimensionality was presented and discussed using a parametric model embedding approach. This allows to reduce the design-space dimensionality before solving the design optimization and/or train the surrogate model. A prescribed (or arbitrary) level of the original design variability is retained (resolved) by the reduced-dimensionality representation. In the multi-fidelity context the method provides an additional fidelity level for the representation of hull geometries in the design space.

Finally, it is worth noting that as each framework is unique in the way that it utilizes specific physical models and numerical solvers, multi-fidelity tools, and parametrization approaches, a direct comparison of capabilities and results encounters a number of barriers. These stem from CAD and CFD tools availability and licences associated to proprietary software, to heterogeneous availability of CPU hours and men power across Team Members. For these reasons, L1 and L2 benchmark problems are devoted to closer comparisons of approaches and results, whereas L3 benchmark problems (at least for the sea case) are dedicated to demonstrating MF methods capabilities for more complex industrial problems, albeit with limited comparison. The possible extension of direct comparison of multi-fidelity design methods to L3 type of problems will be addressed in the future. Nevertheless, **the current discussion within the AVT-331 Sea Team identified promising future research directions**, such as: (i) the use of non-hierarchical approaches, when high-fidelity physical models with coarse discretizations are used in combination with lower-fidelity models with fine discretizations; (ii) the collaborative solution of the same design problem, where distributed high- and low-fidelity computations are distributed among participants, possibly leveraging parallel infill approaches; (iii) the assessment of the relationship between geometric variance and performance variability, along with the development and application of nonlinear approaches to shape reparameterization; finally (iv) the extension of simulation-driven design optimization to incorporate emerging machine learning and artificial intelligence methods, whose effective and efficient integration in the current context needs deeper investigations.

ACKNOWLEDGMENTS

The present research is conducted in collaboration with “AVT-331 Research Task Group on Goal-driven, multi-fidelity approaches for military vehicle system-level design”. CNR-INM’s Framework A optimization tools were mostly developed under Office of Naval Research support, through NICOP grant N62909-18-1-2033, administered by Dr. Woei-Min Lin, Dr. Elena McCarthy, and Dr. Salahuddin Ahmed of the Office of Naval Research and Office of Naval Research Global. Framework B studies of ITU is partially supported by TUBITAK via "Energy Saving Techniques for Energy Efficient Vessels and Emission Reduction towards Green Shipping" project with grant number 218M487.

REFERENCES

[1] A. Serani, M. Diez, F. van Walree, and F. Stern, "Urans analysis of a free-running destroyer sailing in irregular stern-quartering waves at sea state 7," *Ocean Engineering*, vol. 237, p. 109 600, 2021.

[2] P. S. Beran, D. Bryson, A. S. Thelen, M. Diez, and A. Serani, "Comparison of multi-fidelity approaches for military vehicle design," in *AIAA AVIATION 2020 FORUM*, 2020, p. 3158.

[3] A. Olivieri, F. Pistani, A. Avanzini, F. Stern, and R. Penna, "Towing tank, sinkage and trim, boundary layer, wake, and free surface flow around a naval combatant INSEAN 2340 model," DTIC, Tech. Rep., 2001.

[4] H. Sadat-Hosseini, D. H. Kim, S. Toxopeus, M. Diez, and F. Stern, "Cfd and potential flow simulations of fully appended free running 5415m in irregular waves," in *World Maritime Technology Conference, Providence, RI, Nov*, 2015, pp. 3–7.

[5] A. Serani, G. Fasano, G. Liuzzi, *et al.*, "Ship hydrodynamic optimization by local hybridization of deterministic derivative-free global algorithms," *Applied Ocean Research*, vol. 59, pp. 115–128, 2016, ISSN: 0141-1187.

[6] G. Grigoropoulos, E. F. Campana, M. Diez, *et al.*, "Mission-based hull-form and propeller optimization of a transom stern destroyer for best performance in the sea environment," in *Proceedings of the VII International Congress on Computational Methods in Marine Engineering-MARINE*, 2017.

[7] A. Serani, F. Stern, E. F. Campana, and M. Diez, "Hull-form stochastic optimization via computational-cost reduction methods," *Engineering with Computers*, vol. 38, pp. 2245–2269, 2022.

[8] A. Serani and M. Diez, "Parametric model embedding," *arXiv preprint arXiv:2204.05371*, 2022.

[9] T. W. Sederberg and S. R. Parry, "Free-form deformation of solid geometric models," in *Proceedings of the 13th annual conference on Computer graphics and interactive techniques*, 1986, pp. 151–160.

[10] H. Akima, "A method of bivariate interpolation and smooth surface fitting for irregularly distributed data points," *ACM Transactions on Mathematical Software (TOMS)*, vol. 4, no. 2, pp. 148–159, 1978.

[11] M. Diez, E. F. Campana, and F. Stern, "Design-space dimensionality reduction in shape optimization by Karhunen–Loève expansion," *Computer Methods in Applied Mechanics and Engineering*, vol. 283, pp. 1525–1544, 2015.

[12] J. Huang, P. M. Carrica, and F. Stern, "Semi-coupled air/water immersed boundary approach for curvilinear dynamic overset grids with application to ship hydrodynamics," *International Journal for Numerical Methods in Fluids*, vol. 58, no. 6, pp. 591–624, 2008.

[13] G. Vaz, F. Jaouen, and M. Hoekstra, "Free-surface viscous flow computations: Validation of urans code fresco," in *International Conference on Offshore Mechanics and Arctic Engineering*, vol. 43451, 2009, pp. 425–437.

[14] C. M. Klaij and C. Vuik, "Simple-type preconditioners for cell-centered, colocated finite volume discretization of incompressible reynolds-averaged navier–stokes equations," *International Journal for Numerical Methods in Fluids*, vol. 71, no. 7, pp. 830–849, 2013. DOI: https://doi.org/10.1002/fld.3686.

[15] V. Venkatakrishnan, "On the accuracy of limiters and convergence to steady state solutions," in *31st Aerospace Sciences Meeting*, 1993, p. 880.

[16] P. Spalart and S. Allmaras, "A one-equation turbulence model for aerodynamic flows," in *30th aerospace sciences meeting and exhibit*, 1992, p. 439.

[17] F. R. Menter, "Two-equation eddy-viscosity turbulence models for engineering applications," *AIAA journal*, vol. 32, no. 8, pp. 1598–1605, 1994.

[18] R. B. Langtry and F. R. Menter, "Correlation-based transition modeling for unstructured parallelized computational fluid dynamics codes," *AIAA journal*, vol. 47, no. 12, pp. 2894–2906, 2009.

[19] J.-s. Yue and S.-p. Wu, "An improvement to the kunz preconditioner and numerical investigation of hydrofoil interactions in tandem," *International Journal of Computational Fluid Dynamics*, vol. 32, no. 4-5, pp. 167–185, 2018.

[20] C. W. Dawson, "A practical computer method for solving ship-wave problems," in *Proceedings of the 2nd International Conference on Numerical Ship Hydrodynamics*, Berkeley, 1977, pp. 30–38.

[21] H. Schlichting and K. Gersten, *Boundary-Layer Theory*. Springer-Verlag, Berlin, 2000.

[22] P. Bassanini, U. Bulgarelli, E. F. Campana, and F. Lalli, "The wave resistance problem in a boundary integral formulation," *Surveys on Mathematics for Industry*, vol. 4, pp. 151–194, 1994.

[23] J. J. Maisonneuve, "Resolution du probleme de la resistance de vagues des navire par une metode de singularities de rankine," Ph.D. dissertation, University of Nantes, 1989.

[24] B. H. Cheng, "Computations of 3d transom stern flows," in *Proceedings 5th Int. Conf. on Num. Ship Hydrodynamics, Hiroshima*, 1989, pp. 522–529.

[25] W. G. Meyers and A. E. Baitis, "SMP84: Improvements to capability and prediction accuracy of the standard ship motion program SMP81," David Taylor Naval Ship Research and Development Center, Tech. Rep. SPD-0936-04, Sep. 1985.

[26] N. Salvesen, E. Tuck, and O. Faltinsen, "Ship motions and sea loads," 1970.

[27] W. Frank, "Oscillation of cylinders in or below the free surface of deep fluids," DAVID W TAYLOR NAVAL SHIP RESEARCH and DEVELOPMENT CENTER, Tech. Rep., 1967.

[28] J. Wackers, R. Pellegrini, M. Diez, A. Serani, and M. Visonneau, "Improving active learning in multi-fidelity hydrodynamic optimization," in *34th Symposium on Naval Hydrodynamics*, 2022.

[29] C. Piazzola, L. Tamellini, R. Pellegrini, R. Broglia, A. Serani, and M. Diez, "Comparing multi-index stochastic collocation and multi-fidelity stochastic radial basis functions for forward uncertainty quantification of ship resistance," *Engineering with Computers*, pp. 1–29, 2022.

[30] S. Volpi, M. Diez, N. Gaul, *et al.*, "Development and validation of a dynamic metamodel based on stochastic radial basis functions and uncertainty quantification," *Structural and Multidisciplinary Optimization*, vol. 51, no. 2, pp. 347–368, 2015, ISSN: 1615-147X.

[31] A. Serani, R. Pellegrini, R. Broglia, J. Wackers, M. Visonneau, and M. Diez, "An adaptive n-fidelity metamodel for design and operational-uncertainty space exploration of complex industrial problems," in *VIII International Conference on Computational Methods in Marine Engineering MARINE*, 2019.

[32] J. Wackers, M. Visonneau, S. Ficini, R. Pellegrini, A. Serani, and M. Diez, "Adaptive n-fidelity metamodels for noisy cfd data," in *AIAA AVIATION 2020 FORUM*, 2020, p. 3161.

[33] A. Serani, R. Pellegrini, J. Wackers, *et al.*, "Adaptive multi-fidelity sampling for cfd-based optimisation via radial basis function metamodels," *International Journal of Computational Fluid Dynamics*, vol. 33, no. 6-7, pp. 237–255, 2019.

[34] M. A. Bouhlel, N. Bartoli, A. Otsmane, and J. Morlier, "Improving kriging surrogates of high-dimensional design models by partial least squares dimension reduction," *Structural and Multidisciplinary Optimization*, vol. 53, no. 5, pp. 935–952, 2016.

[35] M. C. Kennedy and A. O'Hagan, "Predicting the output from a complex computer code when fast approximations are available," *Biometrika*, vol. 87, no. 1, pp. 1–13, 2000.

[36] D. Huang, T. T. Allen, W. I. Notz, and R. A. Miller, "Sequential kriging optimization using multiple-fidelity evaluations," *Structural and Multidisciplinary Optimization*, vol. 32, no. 5, pp. 369–382, 2006.

[37] T. P. Scholcz and J. Klinkenberg, "Hull-shape optimisation using adaptive multi-fidelity kriging," in *NATO-AVT-354 workshop on multi-fidelity methods for military vehicle design*, Varna, Bulgaria, 2022.

[38] R. H. Byrd, P. Lu, J. Nocedal, and C. Zhu, "A limited memory algorithm for bound constrained optimization," *SIAM J. Sci. Comput.*, vol. 16, pp. 1190–1208, 1995.

[39] A. Serani, M. Diez, E. F. Campana, G. Fasano, D. Peri, and U. Iemma, "Globally convergent hybridization of particle swarm optimization using line search-based derivative-free techniques," in *Recent Advances in Swarm Intelligence and Evolutionary Computation*, ser. Studies in Computational Intelligence, X.-S. Yang, Ed., vol. 585, Springer International Publishing, 2015, pp. 25–47, ISBN: 978-3-319-13825-1.

[40] R. Pellegrini, A. Serani, C. Leotardi, U. Iemma, E. F. Campana, and M. Diez, "Formulation and parameter selection of multi-objective deterministic particle swarm for simulation-based optimization," *Applied Soft Computing*, vol. 58, pp. 714–731, 2017.

[41] K. Deb, A. Pratap, S. Agarwal, and T. Meyarivan, "A fast and elitist multiobjective genetic algorithm: Nsga-ii," *Evolutionary Computation, IEEE Transactions on*, vol. 6, no. 2, pp. 182–197, Apr. 2002.

[42] D. D. Goren O Calisal SM, "Mathematical programming basis for ship resistance reduction through the optimization of design waterline," *J. Marine Science and Tech.*, vol. 22, pp. 772–783, 2017.

[43] R. Storn and K. Price, "Differential evolution–a simple and efficient heuristic for global optimization over continuous spaces," *Journal of global optimization*, vol. 11, no. 4, pp. 341–359, 1997.